STRUCTURAL BIOLOGY

Inactivation-mimicking block of the epithelial calcium channel TRPV6

Rajesh Bhardwaj[1]*, Sonja Lindinger[2]*, Arthur Neuberger[3]*, Kirill D. Nadezhdin[3]*, Appu K. Singh[3,4], Micael R. Cunha[5], Isabella Derler[2], Gergely Gyimesi[1], Jean-Louis Reymond[5], Matthias A. Hediger[1†], Christoph Romanin[2†], Alexander I. Sobolevsky[3†]

Epithelial calcium channel TRPV6 plays vital roles in calcium homeostasis, and its dysregulation is implicated in multifactorial diseases, including cancers. Here, we study the molecular mechanism of selective nanomolar-affinity TRPV6 inhibition by (4-phenylcyclohexyl)piperazine derivatives (PCHPDs). We use x-ray crystallography and cryo–electron microscopy to solve the inhibitor-bound structures of TRPV6 and identify two types of inhibitor binding sites in the transmembrane region: (i) modulatory sites between the S1-S4 and pore domains normally occupied by lipids and (ii) the main site in the ion channel pore. Our structural data combined with mutagenesis, functional and computational approaches suggest that PCHPDs plug the open pore of TRPV6 and convert the channel into a nonconducting state, mimicking the action of calmodulin, which causes inactivation of TRPV6 channels under physiological conditions. This mechanism of inhibition explains the high selectivity and potency of PCHPDs and opens up unexplored avenues for the design of future-generation biomimetic drugs.

INTRODUCTION

Transient receptor potential (TRP) channels are transmembrane (TM) proteins that mediate the flux of monovalent and divalent ions across biological membranes (*1*). TRP channels are associated with a variety of genetic and acquired diseases and investigated as important drug targets (*2*). TRPV6, a member of the vanilloid subfamily of TRP channels, is a cation-permeable epithelial channel that is highly selective to calcium (*3*). Since TRPV6 is the principal calcium uptake channel that captures diet-delivered Ca^{2+} ions in the gut, it is involved in the whole-body calcium homeostasis. As a consequence, it plays an important role in maternal-fetal Ca^{2+} transport (*4*, *5*) and bone homeostasis (*6*), while mutations in TRPV6 are linked to transient neonatal hyperparathyroidism (*7*) as well as undermineralization and dysplasia (*8*) of the human skeleton. In addition, changes in TRPV6 expression have been detected in several mouse models of human diseases, including Pendred syndrome, Crohn's-like disease, Lowe syndrome, Dent disease, Gitelman syndrome, and kidney stone disease (*3*). Because of the central role of calcium in the development of cancer (*9*), TRPV6 has also been classified as an oncochannel (*10*). TRPV6 is overexpressed in various types of human cancer cells, including breast, prostate, colon, ovarian, thyroid, endometrial, and leukemia cancer cells (*9*, *11*). Furthermore, in 93% of biopsies, the levels of TRPV6 were elevated more in invasive compared to noninvasive tumor areas (*12*). Correspondingly, TRPV6 inhibitors can potentially be used for the treatment of a broad range of diseases associated with disturbed calcium homeostasis, including TRPV6-rich tumors (*13*–*16*).

Several small-molecule inhibitors of TRPV6, including 2-aminoethoxydiphenyl borate (2-APB; IC_{50} = 71 μM), have been identified, but the majority either are nonspecific or have low potency (*17*–*21*). In contrast, we developed the first small-molecule TRPV6 inhibitors, (4-phenylcyclohexyl)piperazine derivatives (PCHPDs), that are highly selective and have nanomolar affinity (*21*–*23*). Here, we solve x-ray and cryo–electron microscopy (cryo-EM) structures of TRPV6 in complex with several PCHPD inhibitors and identify PCHPD binding sites in the channel's TM domain. Combining our structural data with mutagenesis and biochemical, functional, and computational approaches, we investigate the mechanism of TRPV6 inhibition by PCHPDs. Unprecedented for TRP channels, PCHPDs mimic the action of calmodulin (CaM), which causes inactivation of TRPV6 channels under physiological conditions (*24*, *25*). This inhibition mechanism explains the high selectivity and potency of PCHPDs and can be used as a guide for structure-based drug design.

RESULTS AND DISCUSSION

Functional characterization of TRPV6 inhibition by PCHPDs

Currents through human TRPV6 (hTRPV6) channels transiently expressed in human embryonic kidney–293 (HEK 293) cells were recorded using the whole-cell patch-clamp technique in response to the application of 10 mM Ca^{2+}. For more detailed functional characterization, we chose cis-22a as the most well-studied and representative of PCHPDs. At −74-mV membrane potential, this highly selective PCHPD antagonist produced potent inhibition of hTRPV6-mediated currents with a half-maximal inhibitory concentration (IC_{50}) of 82 ± 25 nM (n = 7) (Fig. 1, A and B). The current-voltage (I-V) curve (Fig. 1C) showed strong inward rectification, typical for TRPV6 channels, and a positive reversal potential (E_{rev}), consistent with their high Ca^{2+} selectivity in the presence and absence of cis-22a. Recovery of hTRPV6-mediated currents from cis-22a inhibition was slow and reached about 80% of their control amplitude after a 7-min washout (fig. S1A). cis-22a inhibited rat TRPV6 (rTRPV6)–mediated currents with similar potency to hTRPV6-mediated currents (Fig. 1D and fig. S1, B and D).

[1]Department of Nephrology and Hypertension and Department of Biomedical Research, University of Bern, Inselspital, Freiburgstrasse 15, CH-3010 Bern, Switzerland. [2]Institute of Biophysics, Johannes Kepler University Linz, Gruberstrasse 40, 4020 Linz, Austria. [3]Department of Biochemistry and Molecular Biophysics, Columbia University, 650 West 168th Street, New York, NY 10032, USA. [4]Department of Biological Sciences and Bioengineering, Indian Institute of Technology, Kanpur 208016, India. [5]Department of Chemistry and Biochemistry, University of Bern, Freiestrasse 3, 3012 Bern, Switzerland.
*These authors contributed equally to this work.
†Corresponding author. Email: matthias.hediger@ibmm.unibe.ch (M.A.H.); christoph.romanin@jku.at (C.R.); as4005@cumc.columbia.edu (A.I.S.)

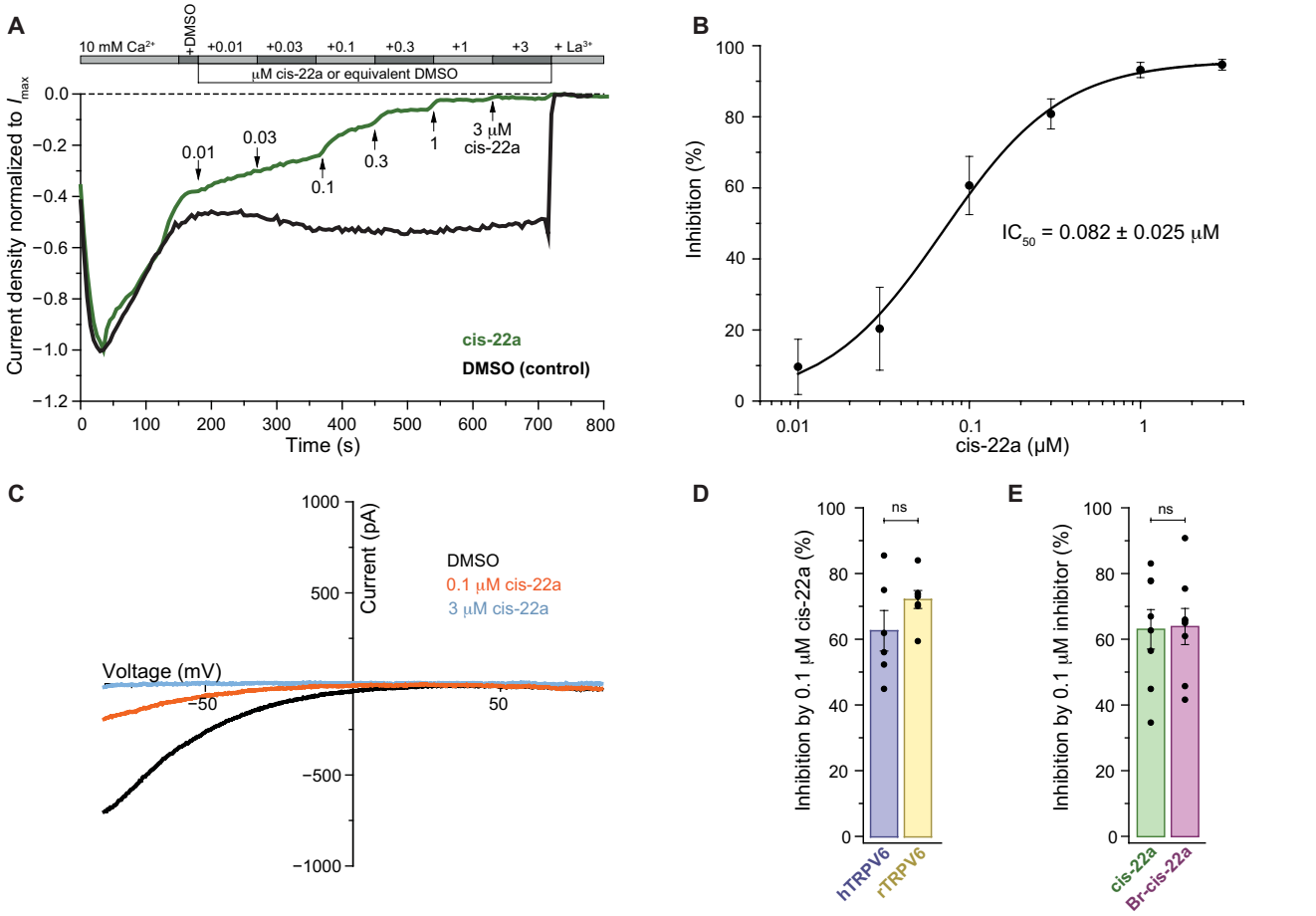

Fig. 1. Functional characterization of TRPV6 inhibition by PCHPDs. (**A**) Representative whole-cell currents recorded from HEK 293 cells expressing hTRPV6 and normalized to their maximal value. Throughout the experiment, 10 mM Ca^{2+} solution was exchanged to the same solution containing the consecutively added dimethyl sulfoxide (DMSO), increasing concentrations of cis-22a (0.01 to 3 μM), and followed by La^{3+}, as indicated by the gray bars. The arrows show time points when cis-22a was added. (**B**) Dose-response curve for hTRPV6 inhibition by cis-22a with calculated IC_{50} (means ± SEM; Hill coefficient, 1.25; $n = 7$). The inhibition was calculated relative to the current in DMSO. (**C**) Representative *I-V* curves before (DMSO) and after addition of cis-22a (0.1 and 3 μM). (**D**) Inhibition of hTRPV6- and rTRPV6-mediated currents (means ± SEM and individual values) by 0.1 μM cis-22a. (**E**) Inhibition of hTRPV6-mediated current (means ± SEM and individual values) by cis-22a and Br-cis-22a at 0.1 μM concentration.

Compared to cis-22a, its diastereomer trans-22a (*21*) showed less potent current inhibition at 10 μM concentration (fig. S1, E to I). We also synthesized Br-cis-22a, a brominated PCHPD analog of cis-22a (see Materials and Methods and fig. S2A). The inhibitory potency of Br-cis-22a, estimated by measuring the uptake of Cd^{2+} into hTRPV6-expressing HEK 293 cells using the calcium-5 fluorescence reporter FLIPR assay (*22*) (IC_{50} = 0.96 ± 0.03 μM; n = 12) (see Materials and Methods and fig. S2B), was also in submicromolar range, comparable to the inhibitory potency of cis-22a (*21*, *23*). Consistently, electrophysiological recordings showed similar extents of hTRPV6 current inhibition by Br-cis-22a and cis-22a at 0.1 and 10 μM concentrations (Fig. 1E and fig. S2, C to E). Our functional experiments, therefore, demonstrated that cis-22a and its brominated analog Br-cis-22a are potent TRPV6 inhibitors.

Inhibitor-bound crystal structure of rTRPV6

To investigate the molecular mechanism of TRPV6 inhibition by PCHPDs, we decided to use x-ray crystallography first. Of several previously developed TRPV6 constructs (*26*–*29*), we chose rTRPV6 construct TRPV6* (see Materials and Methods) that produces well-diffracting crystals and yields structures with the physiologically relevant swapped arrangement of the TM domains (*27*). TRPV6* displays functional behavior similar to wild type but shows no apparent inactivation by CaM because we truncated the C terminus that contains a binding site of CaM (*27*, *30*). As a cocrystallization PCHPD partner of TRPV6*, we chose Br-cis-22a (Fig. 2A), the heavy bromine atom of which anomalously scatters x-rays. Crystals of TRPV6* grown in the presence of Br-cis-22a belonged to the $P42_12$ space group and diffracted to 3.7 Å resolution. We solved the structure of the TRPV6*–Br-cis-22a complex by molecular replacement and built a model that was refined to good crystallographic statistics and stereochemistry (table S1).

The structure of TRPV6*–Br-cis-22a has an architecture typical for the vanilloid subfamily TRP channels. It is composed of (i) a pore-forming TM domain, which includes six TM helices (S1 to S6) and a pore loop (P-loop) between S5 and S6, and (ii) a large intracellular skirt domain with the walls mainly built of ankyrin repeat domains, enclosing a ~50 × 50 Å wide cavity underneath the ion

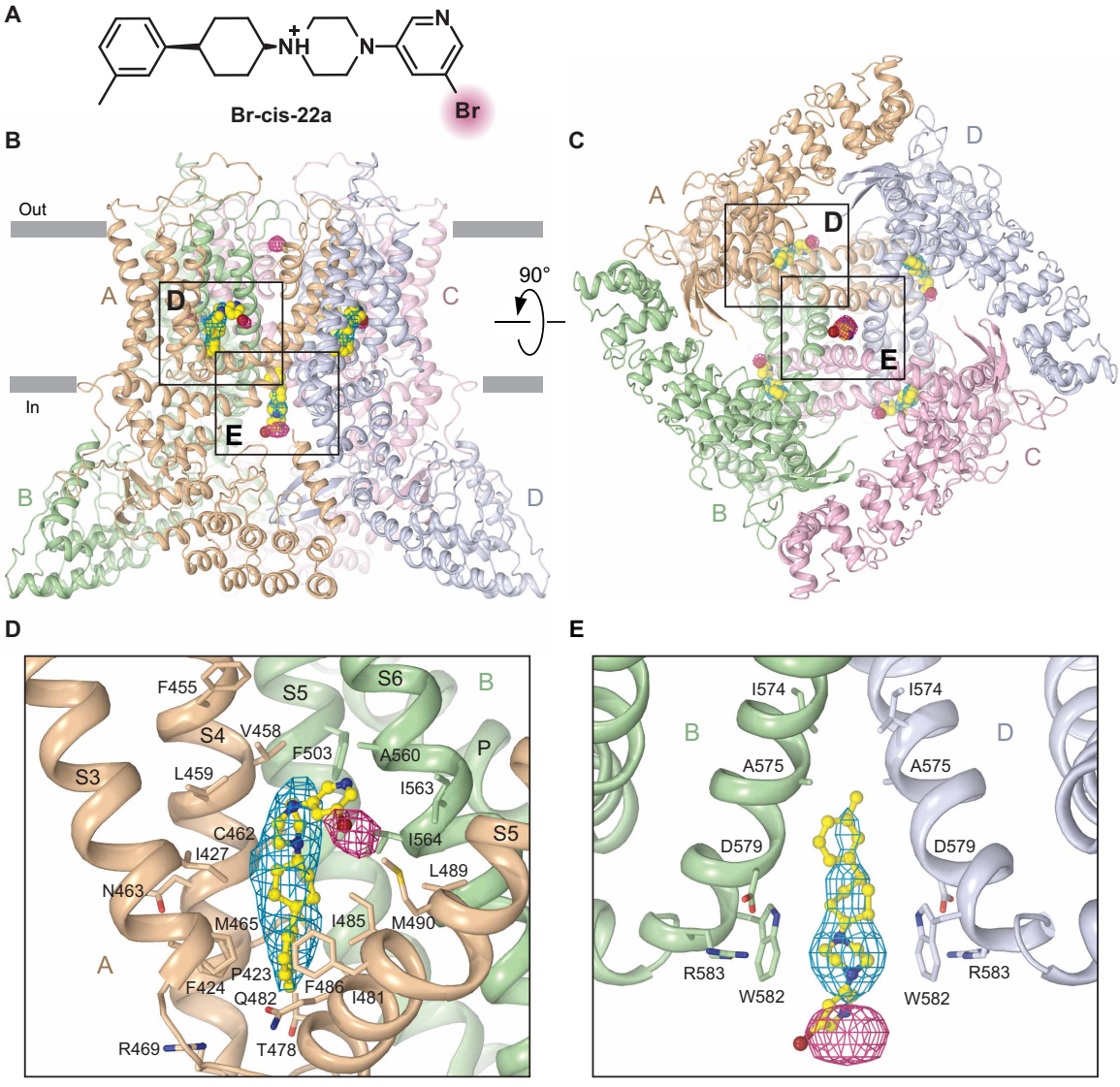

Fig. 2. Crystal structure of inhibitor-bound rTRPV6. (**A**) Chemical structure of the inhibitor Br-cis-22a, with the bromine atom highlighted. (**B** and **C**) Side (B) and bottom (C) views of the rTRPV6 tetramer, with each subunit shown in different color. Molecules of Br-cis-22a are shown in yellow. Mesh shows omit (2.5σ, blue) and anomalous difference (3.0σ, pink) electron density. Boxed are regions expanded in (D) and (E). (**D** and **E**) Close-up views of the lipid-binding site 2 (LBS-2) (D) and the pore binding site (E). Only two of four TRPV6 subunits are shown in (E), with the front and back subunits removed for clarity.

channel (Fig. 2, B and C). Diffraction data collected at 0.92-Å wavelength revealed three types of strong (>4σ) peaks in the anomalous difference Fourier map. The first peak coincides with the main cation binding site at the extracellular entrance to the ion channel selectivity filter formed by the side chains of D541. Since no density of Br-cis-22a shape was observed close to this peak, it likely represents either free residual bromine in the Br-cis-22a sample or a calcium ion that has a small but measurable scattering at 0.92 Å wavelength (f'', ~0.5 e). Confirming the lack of Br-cis-22a binding at this location, attempts to introduce the Br-cis-22a molecule here resulted in strong negative peaks in the $F_o - F_c$ difference map.

The second peak is in close proximity to the lipid-binding site 2 (LBS-2), which was identified in the previous cryo-EM structures of TRPV6 (*29*, *31*). LBS-2 is located in the intracellular half of the lipid membrane bilayer, right above the S4-S5 linker, at the interface between S3, S4, and S4-S5 linker of one subunit and S5 and S6 of the neighboring subunit (Fig. 2D). There is a sausage-like density right next to the second peak that has never been observed in crystal structures of rTRPV6 before (*26*, *27*, *29*). The size and shape of this density suggest a possibility that the LBS-2 is also a binding site for Br-cis-22a, mainly formed by hydrophobic side chains. The third peak in the anomalous difference Fourier map is located at the ion channel intracellular entrance (Fig. 2E). Right next to this peak is a robust density that fits the molecule of Br-cis-22a. Therefore, the ion channel intracellular entrance appears as the second type of binding site where Br-cis-22a acts as a blocker that plugs the pore and physically obstructs ion conductance. To verify the two types of putative PCHPD binding sites identified crystallographically, we applied cryo-EM to hTRPV6.

Cryo-EM structures of hTRPV6

In the crystal structure of TRPV6*–Br-cis-22a, binding of Br-cis-22a at the ion channel intracellular entrance (Fig. 2E) occurs at a similar

location where the CaM lysine K115 side chain blocks the TRPV6 pore during Ca^{2+}-induced inactivation (*30*). It appears that endogenous CaM copurifies with full-length hTRPV6 (hTRPV6-FL) in most of our protein preparations, similar to its copurification with the full-length rTRPV6 that resulted in the rTRPV6-CaM complex structure (*30*). To avoid possible structural interference between the binding of inhibitors and CaM, we truncated the CaM binding site–containing C terminus of hTRPV6, similar to the crystallizing construct TRPV6* (see Materials and Methods). For the resulting construct hTRPV6-CtD, we solved the apo state structure by cryo-EM (Fig. 3A, figs. S3 and S4, and table S2) and found it nearly identical to the previously published apo state structure of hTRPV6-FL (fig. S5) (*31*), with no signs of CaM in the skirt-enclosed cavity underneath the ion channel. We therefore used hTRPV6-CtD to visualize molecular interactions of hTRPV6 with PCHPD inhibitors.

The cryo-EM structure of hTRPV6-CtD solved in the presence of cis-22a (Fig. 3, B and C) revealed two types of nonprotein densities in the TM domain that appear different from densities in the apo state structure (Fig. 3A). They are located at the same two sites (Fig. 3, H and M) that were identified as the putative Br-cis-22a binding sites in the crystal structure of TRPV6*–Br-cis-22a (Fig. 2, D and E). The presence of the central pore site (Fig. 3M) is unambiguous because the density at this site is not present in the apo state structure (Fig. 3A) but observed for all PCHPDs in the corresponding cryo-EM structures (Fig. 3, M to Q). For cryo-EM structures, we did not have the advantage of using anomalous signals to orient the inhibitors at their putative binding sites, as we had for the TRPV6*–Br-cis-22a crystal structure (Fig. 2E). However, given the similarity of PCHPD chemical structures, the same procedures of protein expression and purification for crystallographic and cryo-EM experiments, 100% amino acid sequence identity, and similarity in pore geometry between rat and human TRPV6, we kept the orientation of PCHPDs at the central pore site in cryo-EM structures the same as the orientation of Br-cis-22a in the crystal structure.

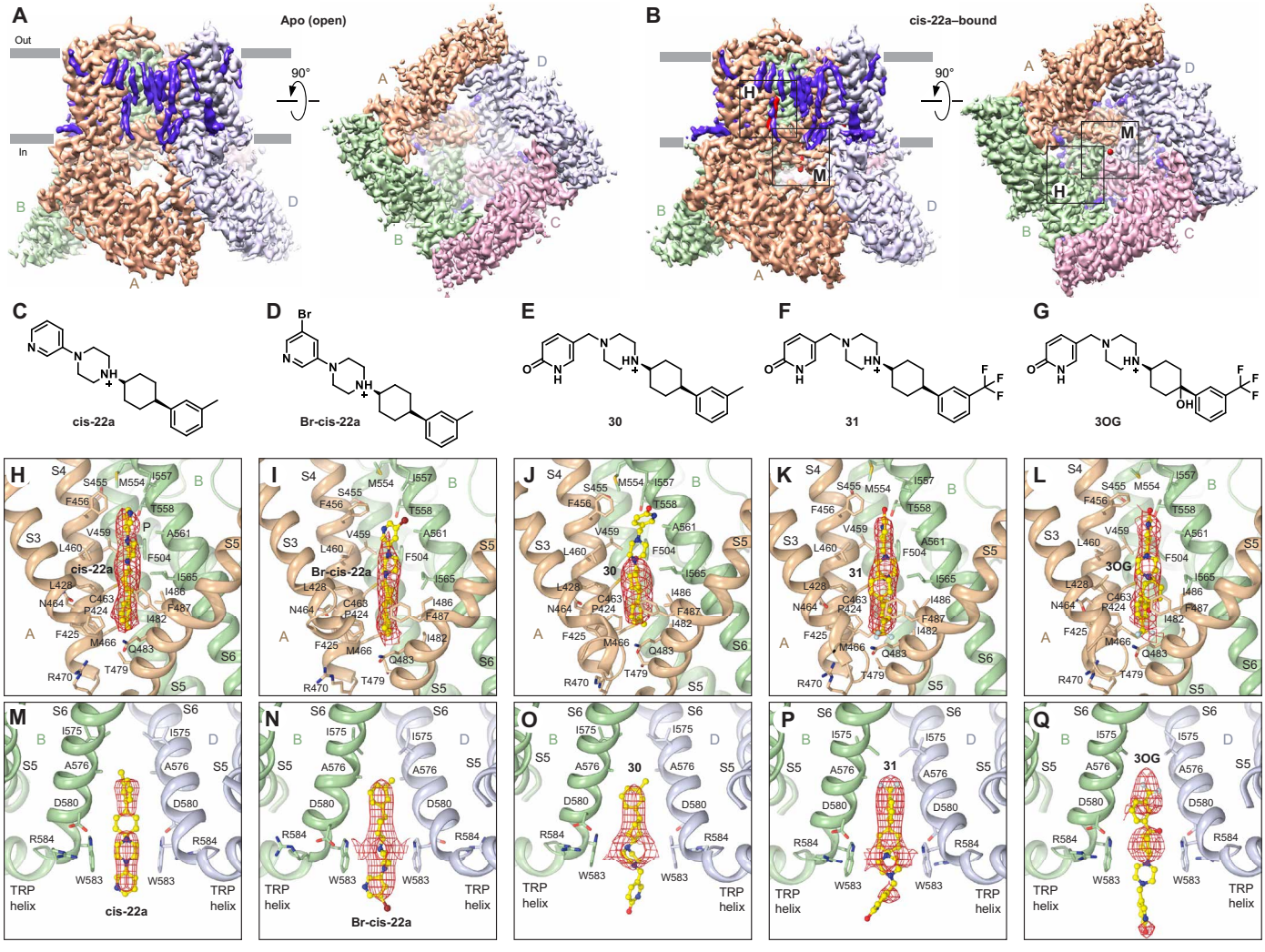

Fig. 3. Cryo-EM structures of hTRPV6 in the absence and presence of different PCHPD inhibitors. (**A** and **B**) Side and bottom views of cryo-EM density for hTRPV6 in the absence of inhibitors (A) and in the presence of cis-22a (B), with each subunit shown in a different color and the inhibitor shown in red. Boxed regions in (B) are expanded in (H) and (M). (**C** to **G**) Chemical structures of different PCHPD inhibitors. (**H** to **Q**) Close-up views of the inhibitor-bound LBS-2 (H to L) and the inhibitor-bound pore binding site (M to Q). In (M) to (Q), only two of four TRPV6 subunits are shown, with the front and back subunits removed for clarity. Red mesh shows densities for different PCHPD inhibitors.

The other putative cis-22a binding site identified by cryo-EM (Fig. 3H) overlaps with LBS-2, which is likely occupied by a cholesterol lipid in natural conditions. In the apo state structure, the LBS-2 density matches the shape of cholesteryl hemisuccinate (CHS), which was present in our experimental buffers (see Materials and Methods and Fig. 4, A and C). The LBS-2 density in the presence of cis-22a is shorter and matches the size and shape of the inhibitor (Fig. 4, B and D). Similar densities were also observed for other PCHPD inhibitors (Fig. 3, I to L). Given different appearances of LBS-2 cryo-EM density in the inhibitor-free and inhibitor-bound structures (Fig. 4) as well as clear signals in the crystallographic anomalous and omit maps of TRPV6* (Fig. 2), our data strongly support the binding of PCHPD inhibitors at the LBS-2. However, we cannot exclude a possibility that occupancy of the LBS-2 by PCHPDs is partial, as they likely compete for binding with the surrounding membrane lipids.

MD simulations of the LBS-2 and the pore binding site

To further verify both LBS-2 and the pore binding site identified by structural methods, we ran molecular dynamics (MD) simulations (see Materials and Methods). The 25-ns MD simulations of cis-22a bound to either the LBS-2 in each monomer of the hTRPV6-CtD tetramer or to the pore binding site indicated a moderate flexibility of the compound within the pockets. Compared to the initial, identical poses of cis-22a bound to LBS-2 in each of the four monomers of the hTRPV6-CtD tetramer determined by the cryo-EM structure, poses obtained during the MD simulations changed very little (fig. S6, A and B). The average root mean square deviations (RMSDs) for cis-22a at the LBS-2 sites were 1.5 to 2.0 Å, whereas the RMSD for the pore-bound compound was 1.6 Å (fig. S6, D and E). The overall conformation of the protein was stable with respect to the final energy-minimized structure. For both simulations, the average Cα RMSD values for the whole protein and TM helices were 3.7 and 2.0 Å, respectively (fig. S6, C and F). To understand whether cis-22a forms a stable interaction with the surrounding residues during the MD simulations, we calculated the average minimum distances between heavy atoms in the residue side chains and cis-22a (table S3). For LBS-2, the minimum distances for residues L460, M466, and Q483 remained below the cutoff (4.0 Å) during the entire MD simulation for all bound cis-22a molecules. Among these, Q483 is the key residue for lipid recognition in TRPV6 (*29*, *31*). It is located in a similar position to E570 in TRPV1 (*32*), an important residue involved in lipid and ligand binding (*32*). The pore binding site is composed of a fewer number of residues compared to LBS-2, but each one of

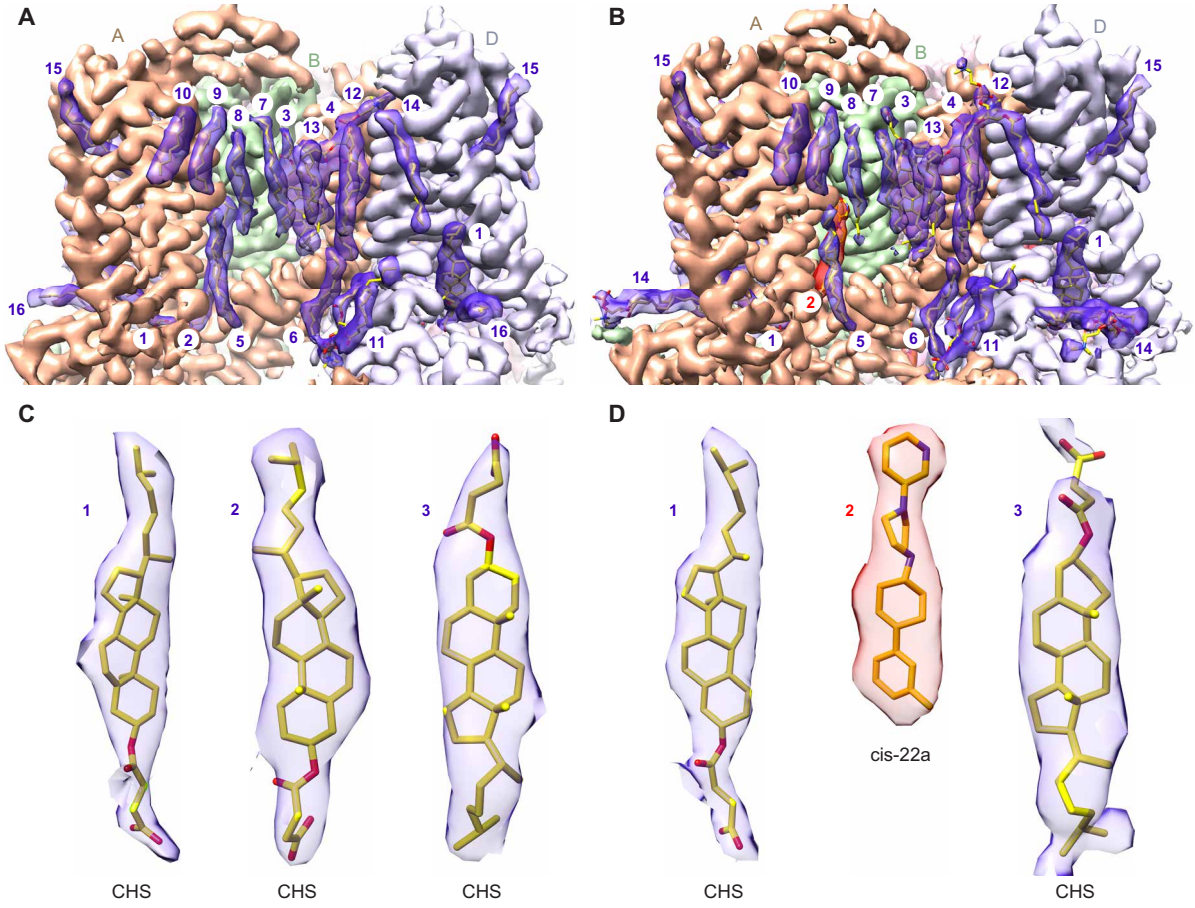

Fig. 4. Nonprotein densities surrounding the TM domain of TRPV6. (**A** and **B**) Side views of cryo-EM density for the TM domain of hTRPV6 in the absence of inhibitors (A) and in the presence of cis-22a (B). Protein density is nontransparent, with each hTRPV6 subunit shown in a different color. Fourteen well-resolved nonprotein densities per subunit of hTRPV6 are transparent, colored purple (lipids), or colored red (cis-22a) and fitted with CHS [sites 1 to 3 in (A) and sites 1 and 3 in (B)], cis-22a [site 2 in (B)], phosphatidylcholine (sites 4 and 11), or acyl chains (sites 5 to 10 and 12 to 14), shown as sticks. (**C** and **D**) Close-up views of density for sites 1 to 3 in the absence of inhibitors (A) and in the presence of cis-22a (B).

four TRPV6 subunits contributes the same set of symmetrically arranged residues. The simulation run highlighted the stability of the complex formed between cis-22a and the central ion channel pore, with minimum distances below 3.0 Å for all analyzed residues. Our MD simulations, therefore, strongly support the two types of PCHPD binding sites in TRPV6 identified by structural methods.

Functional evaluation of the PCHPD pore binding site

To assess the role of the pore site in TRPV6 inhibition by PCHPDs, we mutated the pore-lining residues in close proximity to this site (Fig. 5A) and tested the inhibition of the mutated channels by cis-22a using the FLIPR assay (fig. S7A). HEK 293 cells expressing I575A and D580N mutants showed robust hTRPV6-mediated Cd^{2+} influx, while those transfected with G579A, D580A, D580K, W583A, and R584A mutants showed no detectable Cd^{2+} influx (fig. S7B). The cells transfected with G579A mutant channels showed basal Ca^{2+} levels typical for wild type, while for I575A, D580A/K, W583A, and R584A mutants, the basal Ca^{2+} levels were higher. The fivefold and twofold lower Cd^{2+} influx through hTRPV6 mutants I575A and D580N, respectively, was resistant to inhibition by 0.25 μM cis-22a, which blocked 70% of the wild-type hTRPV6-mediated Cd^{2+} entry (Fig. 5B and fig. S7B). Increasing the concentration of cis-22a to 1 μM resulted in the nearly complete block of Cd^{2+} influx through the wild-type channel but still failed to inhibit Cd^{2+} influx through I575A and D580N mutant channels (fig. S7C). We also tested the effect on Cd^{2+} influx of the recently synthesized PCHPDs inhibitor 3OG, which is among the most promising inhibitors in this class (*23*). We found that 1 μM 3OG showed no inhibition of Cd^{2+} influx through D580N mutant channels, while it inhibited nearly 70% of Cd^{2+} influx through wild-type hTRPV6 channels (fig. S7D). The same concentration of 3OG produced ~15% inhibition of Cd^{2+} entry through I575A mutant channels.

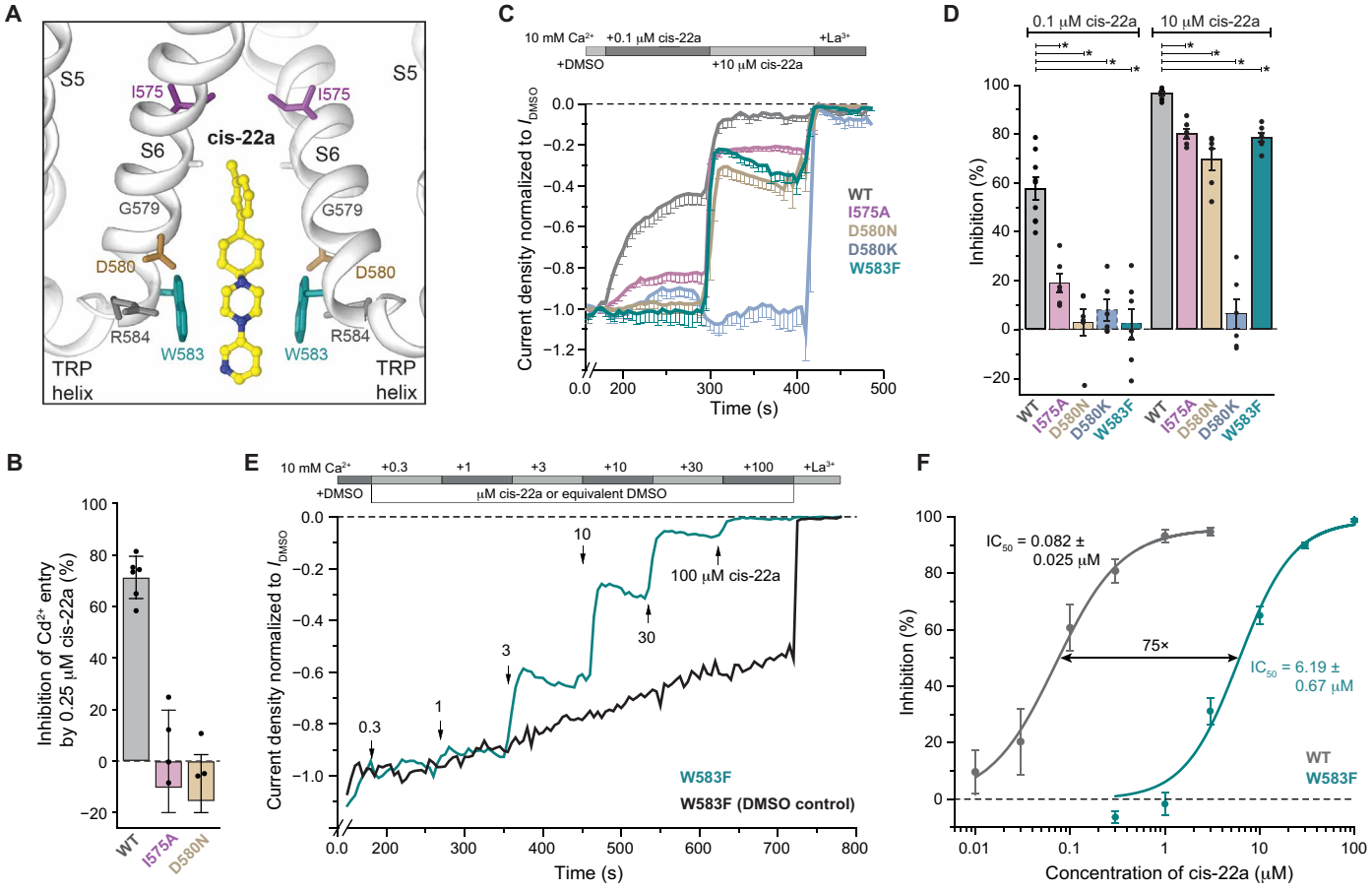

Fig. 5. Functional analysis of the PCHPD pore binding site. (**A**) Schematic view of the PCHPD pore binding site in hTRPV6 bound to cis-22a (yellow), with the surrounding residues shown as sticks. (**B**) Average percentage inhibition of Cd^{2+} entry into HEK 293 cells transiently expressing wild-type hTRPV6, I575A, and D580N pore mutants in response to a 10-min application of 0.25 μM cis-22a, measured using the FLIPR assay ($n = 6$; means ± SD). (**C**) Average amplitude of the whole-cell current (means ± SEM) recorded from HEK 293 cells expressing wild-type hTRPV6 and mutant channels I575A, D580N, D580K, and W583F, normalized to the current amplitude in DMSO (before application of cis-22a). Throughout the experiment, 10 mM Ca^{2+} solution was exchanged to the same solution containing the consecutively added DMSO, cis-22a (0.1 and 10 μM), and followed by Ca^{2+}-free solution containing La^{3+}, as indicated by the gray bars. (**D**) Percent inhibition of wild-type and mutant hTRPV6-mediated currents (means ± SEM and individual values) by 0.1 μM (left) and 10 μM (right) cis-22a. (**E**) Representative whole-cell currents recorded from HEK 293 cells expressing W583F mutant and normalized to the current amplitude in DMSO. Throughout the experiment, 10 mM Ca^{2+} solution was exchanged to the same solution containing the consecutively added DMSO, increasing concentrations of cis-22a (0.3 to 100 μM), and followed by La^{3+}, as indicated by the gray bars. The arrows show time points when cis-22a was added. (**F**) Dose-response curves with calculated IC_{50} for wild-type (means ± SEM; Hill coefficient, 1.25; $n = 7$) and W583F mutant (means ± SEM; Hill coefficient, 1.5; $n = 7$) hTRPV6 channels.

The impact of mutations I575A, D580N, D580K, and W583F at the pore site on hTRPV6 inhibition by PCHPDs was also characterized in electrophysiological experiments by comparing the reduction of currents in response to cis-22a at 0.1 and 10 μM concentrations (Fig. 5, C and D). For wild-type hTRPV6, the application of 0.1 and 10 μM cis-22a resulted in a significant reduction of currents by 57.5 ± 4.6% and 97.2 ± 0.7%, respectively. In contrast, currents through the D580K pore mutant channels were not significantly affected by applications of either 0.1 or 10 μM cis-22a. The pore mutant W583F, which had shown measurable inhibition of currents by cis-22a, was further chosen for the detailed comparison with wild-type hTRPV6. Currents through the W583F channels were not significantly altered by 0.1 μM cis-22a but showed a 79.1 ± 1.7% reduction in response to 10 μM cis-22a application. The *I-V* curve for W583F (fig. S7I) displayed a positive E_{rev}, in line with unaltered calcium selectivity of the mutant channel. The cis-22a dose-response curve for W583F yielded an IC_{50} value of 6.19 ± 0.67 μM (n = 7), indicative of a 75-fold lower affinity of cis-22a to W583F compared to wild-type channels (Fig. 5, E and F, and fig. S7, F and G). This dramatic reduction in cis-22a affinity is likely underestimated, as the correction for the slow reactivation of currents at high concentrations of cis-22a (Fig. 5E) would increase the IC_{50} value for W583F even more. Therefore, the strong functional effects of mutations at the intracellular pore entrance corroborated the importance of the structurally resolved pore site for TRPV6 inhibition by PCHPDs.

Functional evaluation of the LBS-2

To address the role of LBS-2 in TRPV6 inhibition by PCHPDs, we mutated several residues in close proximity to this site (Fig. 6A). Those hTRPV6 mutants that mediated an easily measurable Cd^{2+} influx (20% or higher compared to wild-type channels) were analyzed for inhibition by cis-22a (fig. S7E). In response to the application of 0.25 μM cis-22a, the R470A mutant showed a fivefold reduction in the Cd^{2+} influx inhibition by cis-22a compared to the wild-type channel, whereas for R470K, the reduction was only modest (Fig. 6B). Both Q483A and Q483K mutants showed more than 1.5-fold reduced inhibition of the Cd^{2+} influx by 0.25 μM cis-22a compared to wild-type channels. In addition, a modest but significant reduction in Cd^{2+} influx inhibition by 0.25 μM cis-22a was observed for C463T and N464S mutants of hTRPV6 compared to the wild-type channel.

Four LBS-2 mutants, N464L, R470A, Q483A, and F504Y, were further analyzed electrophysiologically. In response to the application of 0.1 μM cis-22a, all these mutants showed significantly reduced cis-22a inhibition compared to wild type, especially N464L and R470A (Fig. 6, C and D). In general, however, the reduction of cis-22a inhibition demonstrated by the LBS-2 mutants was much weaker than the one caused by mutations at the pore site. The R470A mutation (*31*) was analyzed in more detail. The *I-V* curve for R470A displayed a typical TRPV6 inward current rectification (fig. S7H), while the cis-22a dose-response curve yielded the IC_{50} value of 0.50 ± 0.11 μM, indicating a sixfold lower affinity of the R470A mutant channels to cis-22a compared to wild-type hTRPV6 (Fig. 6, E and F, and fig. S7, F and G).

The strong effects of mutations at the pore intracellular entrance (I575, D580, and W583) on PCHPD inhibition suggest that the pore site is the main PCHPD binding site that mediates TRPV6 channel block. PCHPD binding to the LBS-2 may play an important role in allosteric modulation of the pore binding site, thereby participating in inhibition of the channel function. To further study the role of the two binding sites in TRPV6 inhibition by PCHPDs, we made a double mutant, consisting of the R470A mutation at the LBS-2 and the W583F mutation at the pore site (fig. S8A). In response to the application of 10 μM cis-22a (fig. S8, B and C), the double mutant showed much weaker inhibition of currents compared to the single mutants, indicating that the cumulative effect of R470A and W583F mutations on blocking efficiency is stronger than additive. Thus, the LBS-2 mutations might indirectly affect cis-22 affinity, probably due to the allosteric modulation of the pore binding site. In conclusion, we propose that the pore site is the main PCHPD binding site where the inhibitor plugs the channel and, hence, blocks the ion conductivity.

Inhibitor-induced conformational changes in the ion channel pore

To understand the molecular mechanism of inhibition, we compared the inhibitor-free and inhibitor-bound structures of TRPV6. The overall shape of the channel does not undergo substantial changes upon inhibitor binding (Fig. 3, A and B). However, the ion channel pore shows different conformations in the presence and absence of cis-22a (Fig. 7, A and B). In the apo state (fig. 7A), the calculated pore radius suggests that the lower gate region is wide open for conducting hydrated ions. The pore's most narrow constriction at the gate region is defined by the side chains of I575 (9.9 Å), which constrict the pore to a similar extent as the residues that form the narrowest pore constriction at the intracellular gate region of open TRPV1 (*33*) (interatomic distance of 9.3 Å, measured between the side chains of I679) and TRPV3 (*34*, *35*) (interatomic distance of 8.7 to 9.7 Å, measured between the side chains of I674). The pore-lining S6 segments, which are entirely α-helical in the closed state, show a local α-helical–to–π-helical transition associated with channel opening (*31*). In the presence of cis-22a, the α-to-π transition in S6 remains intact, but the pore becomes markedly narrower as the lower portions of S6 helices are pulled back toward the center of the pore, likely attracted by the inhibitor wedged in the middle (Fig. 7B). The pore's narrow constriction at the gate region is still defined by the side chains of I575, but its smaller size (5.8 Å) suggests the formation of a hydrophobic seal impermeable for ions. This hydrophobic seal is not necessary to prevent ion conduction through the pore, as it is already blocked by cis-22a (Fig. 3M), but it may be important to energetically stabilize the inhibited state.

Inactivation-mimicking mechanism of TRPV6 inhibition by PCHPDs

The PCHPD-induced conformational changes in the TRPV6 pore (Fig. 7, A and B) are very different from the expected conversion of the open channel to its closed state, which is characterized by α-helical S6 and a distinct pore profile (Fig. 7C) (*31*), as previously observed for the inhibitor 2-APB (*29*). Instead, the PCHPD-induced conformational changes are similar to those observed in TRPV6 structures inactivated by CaM (*30*). The side chain of CaM residue K115 in the TRPV6-CaM complex (Fig. 7D) plugs the ion channel intracellular entrance in a similar way to cis-22a (Fig. 7E). Superposition of the two structures (Fig. 7F) clearly shows that the different stimuli result in nearly identical conformations of the lower pore of TRPV6. Tryptophan W583, which is highly conserved across TRPV5 and TRPV6 channels (*30*), plays a central role in K115 binding and CaM inactivation. Four of these tryptophan residues, one from each subunit of

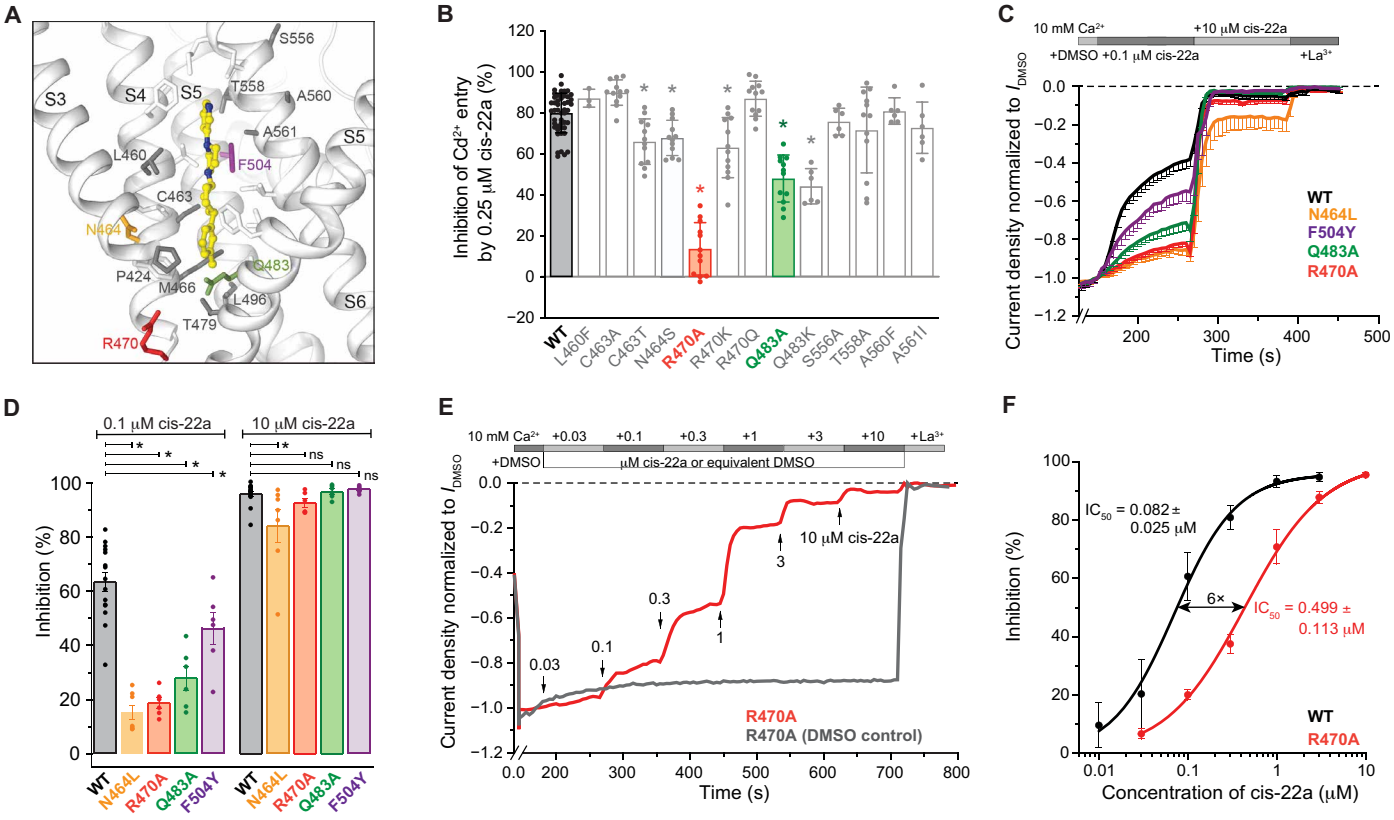

Fig. 6. Functional analysis of the LBS-2. (**A**) Schematic view of the LBS-2 in hTRPV6 bound to cis-22a (yellow), with the surrounding residues shown as sticks. (**B**) Average percentage inhibition of Cd^{2+} entry into HEK 293 cells transiently expressing wild type hTRPV6 and LBS-2 mutants in response to 10-min application of 0.25 μM cis-22a, measured using the FLIPR assay ($n \geq 6$ except for L460F where $n = 3$; means ± SD). Statistically significant difference in inhibition of the mutant compared to the wild-type channels is indicated by "*" ($P < 0.001$). (**C**) Averaged amplitude of whole-cell currents (means ± SEM) recorded from HEK 293 cells expressing wild-type hTRPV6 and mutant channels N464L, R470A, Q483A, and F504Y, normalized to the current amplitude in DMSO (before application of cis-22a). Throughout the experiment, 10 mM Ca^{2+} solution was exchanged to the same solution containing the consecutively added DMSO, cis-22a (0.1 and 10 μM), and followed by Ca^{2+}–free solution containing La^{3+}, as indicated by the gray bars. (**D**) Percent inhibition of wild-type and mutant hTRPV6-mediated currents (means ± SEM and individual values) by 0.1 (left) and 10 (right) μM cis-22a. (**E**) Representative whole-cell currents recorded from HEK 293 cells expressing R470A mutant and normalized to the current amplitude in DMSO. Throughout the experiment, 10 mM Ca^{2+} solution was exchanged to the same solution containing the consecutively added DMSO, increasing concentration of cis-22a (0.03 to 10 μM), and followed by La^{3+}, as indicated by the gray bars. The arrows show time points when cis-22a was added. (**F**) Dose-response curves for wild-type and R470A mutant hTRPV6 channels fitted by the logistic equation (means ± SEM; Hill coefficient, 1.25 and 0.98 for wild type and R470A, respectively).

TRPV6, form a tight cubic cage with 4.2 Å between the plane of each indole ring and the ε-amino group of K115. This tryptophan cage provides a unique environment for an atypically strong cation-π interaction between the π-system of four tryptophan indole rings and the positively charged ε-amino group of lysine. The importance of W583 for CaM-dependent Ca^{2+}-induced inactivation has been demonstrated in experiments with TRPV5, where the W583A mutation has resulted in cell death due to increased calcium influx (*36*). Mutations of W583 to leucine and alanine greatly reduced CaM-mediated inactivation of TRPV5 and converted the channel into the open state (*37*, *38*). Tryptophan W583 seems to also be crucial for TRPV6 inhibition by PCHPDs as the W583F mutation resulted in significant reduction of cis-22a inhibition (Fig. 5, C to F).

The W583F mutation also alters the inactivation behavior of TRPV6 (fig. S9). Wild-type TRPV6 exhibits inactivation visible as a time-dependent decrease in the current amplitude to about 50 to 70% of its maximum value over the first ~180 s of the electrophysiological experiment (fig. S9, B and E). This inactivation is calcium dependent, as it is eliminated upon replacement of the 10 mM Ca^{2+}-containing solution with the divalent-free sodium-containing solution (DVF) (fig. S8, D to F). However, the type of the current carrier, sodium or calcium, does not seem to be important for TRPV6 inhibition by PCHPD since the IC_{50} for cis-22a–induced inhibition of sodium currents (0.178 ± 0.067 μM) is not significantly different from calcium currents (fig. S8, G and H). In contrast, the degree of calcium-dependent inactivation is strongly affected by mutations that alter PCHPD inhibition. Among all these mutations, the reduction of inactivation caused by W583F is relatively moderate (fig. S9, A to C). This is likely due to the phenol rings of phenylalanine W583F, which, similar to indole rings of tryptophans W583, are capable of creating a π-system that can form a cation-π interaction with the positively charged ε-amino group of lysine K115 (Fig. 7D). Other mutations, which weakened PCHPD inhibition, exhibited a stronger reduction of inactivation, independent of whether they were introduced at the pore site (fig. S9, A to C) or LBS-2 (fig. S9, D to F). At the same time, all these mutants had current amplitudes and *I-V* curves comparable to wild-type channels (fig. S10 and Fig. 1C). Our results therefore suggest that any alterations in

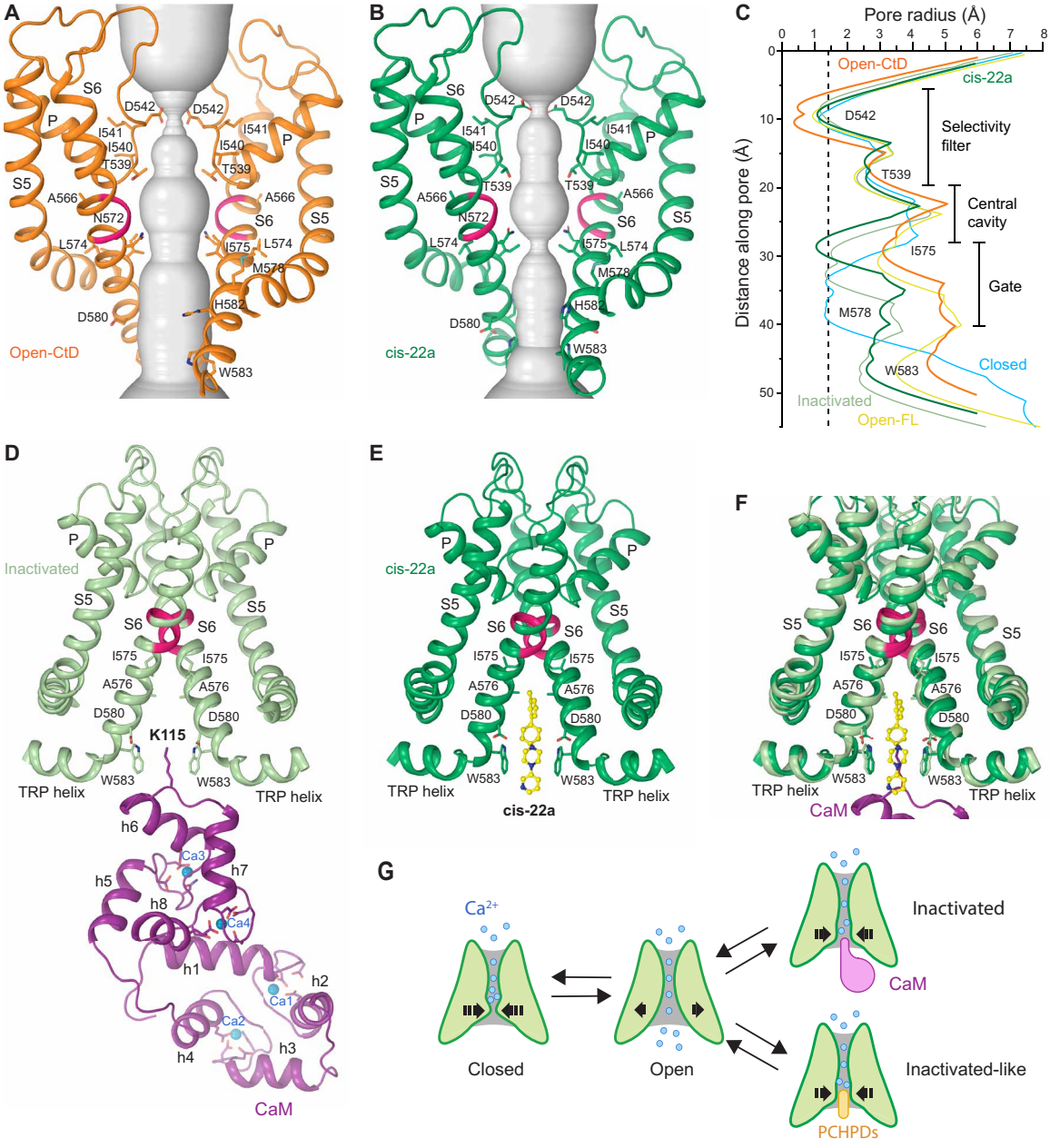

Fig. 7. Comparison of TRPV6 structures in the open state, inhibited by cis-22a and inactivated by CaM. (**A** and **B**) Ion conduction pathway (gray) in the absence of inhibitors (A) and in the presence of cis-22a (B), with residues lining the selectivity filter and around the gate shown as sticks. Only two of four subunits are shown, with the front and back subunits removed for clarity. The π-bulge in the middle of the S6 helices is colored in pink. (**C**) Pore radius calculated using HOLE (*62*) for hTRPV6-CtD in the absence of inhibitors (orange) and in the presence of cis-22a (dark green) and for the hTRPV6-FL in the closed (cyan, hTRPV6-R470E; PDB ID: 6BOA), open (yellow, hTRPV6; PDB ID: 6BO8), and inactivated (light green, hTRPV6-CaM; PDB ID: 6E2F) states. (**D** to **F**) Pore domains in hTRPV6 structures inactivated by CaM (D), bound to cis-22a (E), and their superposition (F). Only two of four hTRPV6 subunits are shown, with the front and back subunits removed for clarity. Molecules of cis-22a and CaM are colored yellow and purple, respectively. Calcium ions are shown as blue spheres. Side chains of residues lining the binding sites for cis-22a, CaM and calcium, and CaM residue K115 are shown as sticks. The π-bulge in the middle of the S6 helices is colored in pink. (**G**) Cartoon illustrating the mechanism of TRPV6 inhibition by PCHPDs.

the pore geometry, whether they are caused by direct changes in the pore composition or via allosteric modulation, affect both the PCHPD inhibition and calcium-dependent inactivation and emphasize the common molecular origin of the two processes.

A number of recently reported x-ray and cryo-EM structures of TRP channels provide insights into the mechanisms of their permeation and modulation by endogenous ligands, natural products, and drug-like small molecules (table S4) (*39*). Most inhibition and activation mechanisms reported to date involve a displacement of endogenous ligands (e.g., ATP and lipids) (*31*) from their respective binding sites, leading to stabilization of either the open (activation) or closed (inhibition) states of the channel (*32*, *40*). In particular, a number of small-molecule inhibitors (e.g., cannabidiol, capsazepine, and econazole) (*32*, *41*, *42*) displace the endogenous activating

lipids (*29*, *42*) from the S4-S5 pocket. In this regard, the high-affinity inactivation-mimicking TRPV6 inhibition by PCHPDs has no precedent among TRP channels. It is also unique for ion channels overall because the structural mechanism of inactivation by CaM has so far been characterized for TRPV6 and TRPV5 channels only (*30*, *37*, *38*). By using this mechanism of the evolutionary optimized physiological function of inactivation, the usage of PCPHD inhibitors as drugs might be less invasive, more compatible with natural processes, and, therefore, more effective and bear less adverse side effects.

In conclusion, PCHPDs are potent and selective TRPV6 channel inhibitors that act as inactivation-mimicking pore blockers. Further expansion of this class of biomimetic inhibitors and their in vivo examination will help to proceed with the development of therapeutic substances targeting TRPV6 and possibly other ion channels.

MATERIALS AND METHODS

Synthesis of PCHPDs

cis-22a, 30, 31, and 3OG were synthesized as described previously (*21*). Br-cis-22a was synthesized for x-ray crystallography purposes according to the following procedure (fig. S2A). Briefly, the 1-bromo-3-methylbenzene (**1**) was coupled to 1,4-cyclohexanedione monoethylene acetal (**2**) via Grignard reaction to form the tertiary alcohol (**3**), followed by a multistep procedure to form the required intermediate 4-(m-tolyl)cyclohexan-1-one (**4**). Then, **4** was subjected to reductive amination with 1-(5-bromopyridin-3-yl)piperazine (**5**) to achieve compound Br-cis-22a, which was isolated by column chromatography. After characterization, the freebase was converted into its respective dihydrochloride salt. All commercial reagents were used without further purification. Dry solvents were obtained directly from a drying solvent system. Chromatographic purifications were performed using silica gel (Sigma-Aldrich; 230 to 400 mesh). Automated chromatographic purification was performed with puriFlash 430 system (Interchim) using Teledyne ISCO normal-phase RediSepRf cartridge and detection by ultraviolet absorption (214 nm). Low-resolution mass spectra were obtained by electron spray ionization (ESI), positive mode (Thermo Scientific LCQ Fleet). High-resolution mass spectra were obtained by ESI, positive mode (Thermo Scientific LTQ Orbitrap XL). ^{1}H- and ^{13}C-NMR (nuclear magnetic resonance) spectra were recorded at 300 and 75 MHz, respectively (Bruker AV300). ^{1}H and ^{13}C chemical shifts are quoted relative to solvent signals. MestreNova was used for further analysis of the spectra. The purity of the final compound was >95%, as confirmed by analytical reversed-phase ultrahigh-performance liquid chromatography (RP-UHPLC) with detection at 214 nm, on a Dionex UltiMate 3000 RSLC System (DAD-3000 RS Photodiode Array Detector) and Dionex Acclaim RSLC 120 column (C18; 3.0 × 50 mm; particle size of 2.2 µm; 120 Å pore size) at a flow rate of 1.2 ml/min. Data recording and processing were done with Dionex Chromeleon Management System (version 6.8) and Xcalibur (version 2.2, Thermo Scientific). Eluents for analytical RP-UHPLC were as follows: A, milli-Q deionized water with 0.05% trifluoroacetic acid (TFA); D, HPLC-grade acetonitrile/milli-Q deionized water (9:1) with 0.05% TFA. Conditions for analytical RP-UHPLC were as follows: in 4.5 min from 100% A to 100% D and then maintained on 100% D or in 7.5 min from 100% A to 100% D and then maintained on 100% D. Chemical names were generated using ChemDraw Professional 17.0 (PerkinElmer Informatics). The steps of chemical synthesis are described in more detail below.

Procedure for the synthesis of 8-(m-tolyl)-1,4-dioxaspiro[4.5]decan-8-ol (3)

A solution of 1-bromo-3-methylbenzene (1; 1.2 ml, 1.2 eq) in dry tetrahydrofuran (THF) (1 ml) was added dropwise to magnesium turnings (342.2 mg, 1.4 eq) in dry THF (1.4 ml) at room temperature (r.t.) under argon atmosphere. The solution was then heated to reflux for 30 min until the complete formation of the Grignard reagent. After cooling to r.t., a solution of 1,4-cyclohexanedione monoethylene acetal (**2**; 1.6 g, 1 eq) in dry THF (2.4 ml) was added to the reaction mixture, and the solution was heated again to reflux for 30 min. After cooling to r.t., the reaction was quenched by the addition of an aqueous saturated solution of NH_4Cl (6 ml) and was extracted with Et_2O (3 × 50 ml). The combined organic phase was dried over $MgSO_4$ and evaporated under vacuum. The obtained residue was column-chromatographed (hexanes:EtOAc, 95:05 to 75:25) to yield **3** as white solids (2.3 g; 93%).

Procedure for the synthesis of 4-(m-tolyl)cyclohexan-1-one (4)

TsOH (177 mg, 0.1 eq) was added to a solution of **3** (9.3 mmol, 1 eq) in dry toluene (44 ml) under argon atmosphere, and this solution was heated to reflux for 4 hours. The reaction mixture was cooled to r.t. and washed with an aqueous saturated solution of $NaHCO_3$ (3 × 50 ml). The organic phase was dried over $MgSO_4$ and evaporated under vacuum. The obtained oil was used in the next step without further purification. A solution of the previously obtained compound in EtOAc (20 ml) and 10% Pd/C (229 mg, 0.3 eq) was hydrogenated for 16 hours at r.t. and atmospheric pressure. The reaction mixture was filtered over a pad of Celite (washed thoroughly 3 × 50 ml with EtOAc) to remove the catalyst. The solvent was removed under vacuum, and the crude was used in the next step without further purification (colorless oil). The previously obtained compound was solubilized in a mixture of acetone:water (1:1; 40 ml). To this solution, pyridinium *p*-toluenosulfonate (4.6 g, 2 eq) was added and the mixture was stirred at 60°C for 6 hours. After cooling to r.t., the organic solvent was removed under vacuum and the resulting aqueous phase was extracted with EtOAc (3 × 50 ml). The collected organic phase was dried over Na_2SO_4 and evaporated. The crude was column-chromatographed (hexanes:EtOAc, 9:1) to yield **4** as a colorless oil (1.1 g; 63%). ^{1}H-NMR ($CDCl_3$): δ 7.25 to 7.19 (m, 1H), 7.05 (d, J = 7.5 Hz, 3H), 2.99 (tt, J = 12.1, 3.4 Hz, 1H), 2.58 to 2.48 (m, 4H), 2.36 (s, 3H), 2.25 to 2.18 (m, 2H), 2.02 to 1.87 (m, 2H). ^{13}C-NMR ($CDCl_3$): δ 211.4, 144.9, 138.3, 128.6, 127.6, 127.4, 123.8, 42.9, 41.5, 34.1, 21.6. HRMS (high-resolution mass spectrometry) mass/charge ratio (m/z) calculated for $C_{13}H_{16}O$: 188.1201 ($[M]^+$); found: 211.1091 ($[M + Na]^+$).

Procedure for the synthesis of 1-(5-bromopyridin-3-yl)-4-((1s,4s)-4-(m-tolyl)cyclohexyl)piperazine, double hydrochloride salt (Br-cis-22a)

A solution of **4** (94.2 mg, 1 eq) in DCE (1,2-dichloroethane) (5 ml) was added to 1-(5-bromopyridin-3-yl)piperazine (5; 145.3 mg, 1.2 eq), AcOH (29 µl, 1.0 eq), and $NaBH(OAc)_3$ (127.2 mg, 1.2 eq). The solution was then stirred at r.t. for 48 hours. After completion, monitored by thin-layer chromatography, the organic phase was evaporated and the crude was column-chromatographed (hexanes:EtOAc, 90:10 + 0.5% Et_3N). Last, Br-cis-22a was solubilized in Et_2O and precipitated by addition of a methanol solution of HCl as white powder (99 mg; 41%, white solids). ^{1}H-NMR (CD_3OD): δ 8.42 (d, J = 2.6 Hz, 1H), 8.30 (d, J = 1.6 Hz, 1H), 8.06 (t, J = 2.1 Hz, 1H), 7.23 to 7.19 (m, 3H), 7.01 (t, J = 3.7 Hz, 1H), 4.07 (d, J = 13.6 Hz, 2H), 3.77 (d, J = 11.9 Hz, 2H),

3.47 (dd, J = 12.3, 9.7 Hz, 3H), 3.26 (d, J = 11.3 Hz, 2H), 2.96 (t, J = 6.7 Hz, 1H), 2.36 to 2.28 (m, 5H), 2.10 to 1.85 (m, 6H). ^{13}C-NMR (CD_3OD): δ 149.0, 144.8, 139.2, 136.3, 131.6, 131.2, 129.5, 129.0, 127.8, 125.3, 123.2, 66.3, 49.8, 45.5, 39.2, 29.1, 24.9, 21.6. HRMS *m/z* calculated for $C_{22}H_{29}BrN_3$: 414.1539 ($[M + H]^+$); found: 414.1555.

X-ray crystallography and Cryo-EM

Constructs

The hTRPV6-FL (residues 1 to 725) used for cryo-EM was cloned into a pEG BacMam vector (*43*), with a C-terminal thrombin cleavage site (LVPRG), followed by a streptavidin affinity tag (WSHPQFEK). hTRPV6-CtD (residues 1 to 666) was produced from the hTRPV6-FL construct using standard molecular biology procedures. The TRPV6* construct used for crystallization was similarly made by introducing rTRPV6 into the BacMam vector (*27*). Compared to wild-type rTRPV6, TRPV6* is C-terminally truncated by 59 residues and contains three point mutations in the ankyrin repeat domain (I62Y, L92N, and M96Q).

Expression and purification

TRPV6* and hTRPV6-CtD constructs were expressed and purified as previously described for TRPV6* (*27*) and wild-type hTRPV6 (*31*) with slight modification. Bacmids and baculoviruses were produced using a standard method (*43*). In short, baculovirus was made in Sf9 cells for ~72 hours (Thermo Fisher Scientific, mycoplasma test negative, GIBCO no. 12659017) and was added to the suspension-adapted HEK 293 cells lacking *N*-acetyl-glucosaminyl-transferase I (mycoplasma test negative, ATCC no. CRL-3022) that was maintained in FreeStyle 293 media (Gibco-Life Technologies no. 12338-018) supplemented with 2% fetal bovine serum (FBS) at 37°C and 5% CO_2. Ten to 24 hours after transduction, 10 mM sodium butyrate was added to enhance protein expression, and the temperature was reduced to 30°C. At 48 to 72 hours after transduction, the cells were harvested by centrifugation at 5471*g* for 15 min using a Sorvall Evolution RC centrifuge (Thermo Fisher Scientific), washed in phosphate-buffered saline (pH 8.0), and pelleted by centrifugation at 3202*g* for 10 min using an Eppendorf 5810 centrifuge. The cell pellet was resuspended in ice-cold lysis buffer, containing 20 mM tris-Cl (pH 8.0), 150 mM NaCl, 0.8 μM aprotinin, 4.3 μM leupeptin, 2 μM pepstatin A, 1 mM phenylmethylsulfonyl fluoride, and 1 mM β-mercaptoethanol (βME). Cells were subsequently lysed using a Misonix Sonicator with a preset program (6 cycles of 15 s "on" at the amplitude of 8 followed by 15 s "off"; this program was repeated three times for optimal cell lysis) under constant stirring on ice. Unbroken cells and cell debris were pelleted in an Eppendorf 5810 centrifuge at 3202*g* and 4°C for 10 min. The supernatant was subjected to ultracentrifugation in a Beckman Coulter ultracentrifuge using a Beckman Coulter Type 45 Ti rotor at 186,000*g* and 4°C for 1 hour to pellet the membranes. The membrane pellet was mechanically homogenized and solubilized in the lysis buffer supplemented with 1% (w/v) *n*-dodecyl β-D-maltoside (DDM) and 0.1% (w/v) CHS under stirring at 4°C for 2 hours. Insoluble material was removed by ultracentrifugation for 1 hour in a Beckman Coulter Type 45 Ti rotor at 186,000*g*, and the supernatant was added to strep resin and rotated for 14 to 16 hours at 4°C. Next, the resin was washed with 10 column volumes of wash buffer containing 20 mM tris-HCl (pH 8.0), 150 mM NaCl, 1 mM βME, 0.01% (w/v) glyco-diosgenin (GDN), and 0.001% (w/v) CHS, and the protein was eluted with the same buffer supplemented with 2.5 mM D-desthiobiotin. The eluted protein was concentrated using a 100-kDa NMWL (nominal molecular weight limit) centrifugal filter (MilliporeSigma Amicon) to 0.5 ml and then centrifuged in a Sorvall MTX 150 micro-ultracentrifuge (Thermo Fisher Scientific) using a S100AT4 rotor for 30 min at 66,000*g* and 4°C before injecting into a size exclusion chromatography (SEC) column. All constructs were further purified using a Superose 6 10/300 GL SEC column attached to an AKTA FPLC (fast protein liquid chromatography) (GE Healthcare) and equilibrated in 150 mM NaCl, 20 mM tris-HCl (pH 8.0), 1 mM βME, 0.01% GDN, and 0.001% CHS. The tetrameric peak fractions were pooled and concentrated using a 100-kDa NMWL centrifugal filter (MilliporeSigma Amicon) to 2 to 4 mg/ml.

All PCHPD inhibitors were dissolved in dimethyl sulfoxide (DMSO) to a concentration of 10 mM. The inhibitor cis-22a was further diluted in buffer containing 20 mM tris-HCl (pH 8.0), 150 mM NaCl, 1 mM βME, 0.01% GDN, and 0.001% CHS to a concentration of 2.5 mM. All PCHPD inhibitors were added to the protein 30 min before grid preparation or crystallization at the final concentration of 1 mM (Br-cis-22a, 3OG, 30, and 31) or 0.5 mM (cis-22a).

Crystallization and structure determination

Purified TRPV6* protein was concentrated to ~2.5 mg/ml. After the addition of 1 mM Br-cis-22a inhibitor (10 mM stock in DMSO), the protein was incubated for ~30 min on ice and ultracentrifuged (Ti 100 rotor, 86,500*g*, 40 min, 4°C) to get rid of any aggregated material. Crystals of TRPV6* were grown in the hanging drop configuration at 20°C in the reservoir solution containing 20 to 24% PEG 350 MME (methoxypolyethylene glycol, molecular weight 350), 50 mM NaCl, 50 mM tris-HCl (pH 8.0 to 8.5), and 10 mM ammonium formate. They were cryoprotected by serial transfer into buffers composed of 100 mM NaCl, 100 mM tris-HCl (pH 8.2), 0.5 mM DDM, 10 mM ammonium formate, and increasing concentrations of PEG 350 MME with the maximum concentration of 33 to 36% and then flash-frozen in liquid nitrogen. X-ray diffraction data collected at The Advanced Photon Source (in Argonne, Illinois, USA) (beamline 24-ID-C) were indexed, integrated, and scaled using XDS (*44*). The initial phase information was obtained and the TRPV6*–Br-cis-22a structure was solved by molecular replacement using Phaser (*45*), for which the structure of TRPV6* (PDB ID: 5WO7) (*27*) served as a search probe. The structure was further improved by alternating cycles of refinement in Phenix (*46*) and model building in Coot (*47*).

Cryo-EM sample preparation and data collection

Au/Au grids were prepared as described in the literature (*48*). Briefly, grids were prepared by first coating C-flat (Protochips Inc., Morrisville, NC) CF-1.2/1.3-2Au mesh holey carbon grids with ~60 nm of gold using an Edwards Auto 306 evaporator. Subsequently, an Ar/O_2 plasma treatment [4 min, 50 W, 35.0 sccm (standard cubic centimeters per minute) of Ar, 11.5 sccm of O_2] was used to remove the carbon with a Gatan Solarus (model 950) advanced plasma cleaning system (Gatan, Pleasanton, CA, USA). The grids were again plasma-treated (H_2/O_2, 25 s, 10 W, 6.4 sccm of H_2, 27.5 sccm of O_2) before sample application to make their surfaces hydrophilic. A Mark IV Vitrobot (Thermo Fisher Scientific) set to 100% humidity at 4°C was used to plunge-freeze the grids in liquid ethane after applying 3 μl of protein sample to their gold-coated side using a blot time of 3 s, a blot force of 3, and a wait time of 20 s. The grids were stored in liquid nitrogen before imaging.

Images of frozen-hydrated particles of hTRPV6 in the absence of ligands or presence of cis-22a or 31 were collected on a Titan Krios transmission electron microscope (TEM) (Thermo Fisher Scientific) operating at 300 kV and equipped with a post-column GIF Quantum

energy filter and a Gatan K3 Summit direct electron detection (DED) camera (Gatan, Pleasanton, CA, USA) using Leginon (*49*). For hTRPV6 in the presence of cis-22a, 5787 micrographs were collected in counting mode with an image pixel size of 0.83 Å across a defocus range of −1.0 to −2.0 μm. The total dose of ~58 e^- Å^{-2} was attained by using a dose rate of ~16 e^- pixel^{-1} s^{-1} across 50 frames for a 2.5-s total exposure time. For hTRPV6 in the presence of 31, 6270 micrographs were collected with an image pixel size of 0.84 Å and a defocus range of −1.5 to −2.5 μm. For hTRPV6 in the absence of inhibitors, 5732 micrographs were collected with an image pixel size of 0.84 Å and a defocus range of −1.0 to −2.0 μm.

Images of frozen-hydrated particles of hTRPV6 in the presence of 30, 3OG, or Br-cis-22a were collected on a Polara 300 kV TEM (FEI) with a Schottky field emission gun, cartridge loading system, and a Gatan K3 Summit DED camera (Gatan, Pleasanton, CA, USA). For hTRPV6 in the presence of Br-cis-22a, 5787 micrographs were collected in counting mode with an image pixel size of 0.95 Å across a defocus range of −1.5 to −3.5 μm. The total dose of ~71 e^- Å^{-2} was attained by using a dose rate of ~16 e^- pixel^{-1} s^{-1} across 40 frames for 4 s of total exposure time. For hTRPV6 in the presence of 30 and 3OG, 6362 and 7626 micrographs were collected, respectively.

Image processing and 3D reconstruction

All datasets were processed in RELION (*50*) and/or cryoSPARC (see table S2 for details) (*51*). Movies were motion-corrected with either MotionCor2 (*52*) algorithm implemented in RELION (*50*) or cryoSPARC's built-in patch motion correction (*51*). Contrast transfer function (CTF) estimation was performed on non–dose-weighted micrographs using Gctf (*53*) or patch CTF estimation in cryoSPARC (*51*). Subsequent data processing was done on dose-weighted micrographs. Following CTF estimation, micrographs were manually inspected, and those with outliers in defocus values, ice thickness, and astigmatism as well as micrographs with lower predicted CTF-correlated resolution (>6 Å) were excluded from the rest of the processing pipeline (individually assessed for each parameter relative to overall distribution; no set threshold). For this curation, in the case of datasets processed in cryoSPARC (*51*), the exposure curation module was used. Particles were picked (i) manually (in RELION) or (ii) using cryoSPARC's blob picker and, in both cases, further classified into two-dimensional (2D) classes. A selection of 2D classes was used to generate templates for template-based picking. Picked particles were further 2D- and 3D-classified in iterative classification and selection rounds. 3D-selected classes were used for 3D template generation and refinement. The reported resolutions of the final maps were estimated using the gold standard Fourier shell correlation (GSFSC) in cryoSPARC (*51*). The local resolution predictions were calculated in cryoSPARC (*51*), with the resolution range estimated using FSC = 0.143 criterion (*50*). EM density visualization was done in UCSF (University of California at San Francisco) Chimera (*54*).

As a representative of the image processing workflow, data for hTRPV6 in the presence of cis-22a were processed as follows (see also fig. S3). Initially, 1695 particles were manually picked in RELION (*50*) to generate 2D classes that were subsequently used as templates to automatically pick a total of 1,593,044 particles. These particle images were imported into cryoSPARC (*51*) for three iterative rounds of 2D classification and 2D class selection, i.e., with manual selection of 2D classes between classification rounds to further reclassify the selected classes. The particle images from the final 2D selection (329,613 particles) were subjected to 3D classification (heterogeneous refinement in cryoSPARC) into four classes with no symmetry imposed using a box- and pixel-size–corrected, previously published 3.9-Å cryo-EM map of hTRPV6 (EMD-8961) (*30*) as template volume. Particles from three resulting classes (279,260 in total) were pooled together and refined with the C4 symmetry using cryoSPARC's homogeneous refinement, with the imported volume (EMD-8961) as a template, to a 3.19-Å-resolution map. The particle stacks were CTF-refined and then used together with the 3.19-Å map as a template in another round of homogeneous refinement with imposed C4 symmetry to reach a 3.13-Å-resolution map. The same particles were then subjected to a final round of 3D classification into four classes with C4 symmetry using the 3.13-Å map as well as lower-resolution volumes from intermediate 3D homogeneous and heterogeneous refinements as templates to separate particles of different quality. The largest of the resulting four 3D classes (199,015 particles) was homogeneously refined with C4 symmetry using the generated volume from the heterogeneous refinement (3.67 Å map) as template to 3.10 Å.

Model building

To build models of TRPV6 in the absence or presence of PCHPDs in Coot (*47*), we used the previously published crystal or cryo-EM structures of TRPV6 as guides (*27*, *31*). The models were tested for overfitting by shifting their coordinates by 0.5 Å (using shake) in Phenix (*46*), refining each shaken model against a corresponding unfiltered half map, and generating densities from the resulting models in Chimera. Structures were visualized, and figures were prepared in UCSF Chimera (*54*) and PyMOL (*46*).

MD simulations

The 3D structure of cis-22a bound to hTRPV6-CtD reported here was used for MD simulations. The files containing the atomic coordinates of cis-22a bound to hTRPV6-CtD were embedded in a dipalmitoyl phosphatidylcholine (DPPC) bilayer solvated with simple point charge (SPC) water and 0.15 M NaCl (*55*). The bilayer and lipid parameters were downloaded from the web server (http://wcm.ucalgary.ca/tieleman/downloads). To fully embed the structures of the hTRPV6-CtD tetramer on the downloaded lipid bilayer, we used genconf –nbox implemented in Gromacs 2020.1 (*56*) to expand the lipid box through X and Y. The starting system for MD simulations was also assembled with Gromacs 2020.1. For packing lipids around an embedded protein, we used the script InflateGRO (*57*), manually removing the overlapping lipids. For the tetramer-bound system, wherein cis-22a was only retained in the LBS-2 sites, the box dimensions had 12.8 × 12.8 × 12.8 Å, the hTRPV6-CtD tetramer, 4 cis-22a molecules, 335 DPPC molecules, 41,026 SPC water molecules, 207 sodium ions, 191 chloride ions, totaling 165,574 atoms. For the pore-bound system, wherein the cis-22a was only retained in the pore site, the box dimensions had 12.8 × 12.8 × 12.8 Å, the hTRPV6-CtD tetramer, 1 cis-22a molecule, 335 DPPC molecules, 41,015 SPC water molecules, 210 sodium ions, 191 chloride ions, totaling 165,379 atoms.

MD simulations were run using Gromacs 2020.1 with a time step of 2 fs for computation and GROMOS96 53A6 force field, extended to include Berger lipid parameters (*58*). Initial parameters for cis-22a were obtained from the Automated Topology Builder web server (https://atb.uq.edu.au/). The system was first energy-minimized using steepest descent for 1000 steps with position restraints on all protein atoms, ligands, and lipids. Then, another three steps of energy minimization were consecutively followed by

removing the restraint over lipids, ligand, and lastly protein. After energy minimization, 5 ns of isochoric-isothermal (NVT) simulation with position restraint on all protein and ligand atoms was performed at 323 K. The isobaric-isothermal (NPT) equilibration was performed in four steps, consisting of gradually decreasing the positional restraints on the heavy atoms of protein and ligand. First, the system was equilibrated for 5 ns with position restraint on all protein and ligand atoms, at 323 K, then the position restraint was switched to protein backbone and all ligand atoms for 5 ns, then the system was equilibrated for 5 ns with restraints over ligands, and the temperature was switched to 303 K. The last step of NPT equilibration was performed in 5 ns without restraints. The 25-ns production run was also performed without restraints. During the equilibration, system pressure was 1 bar, using velocity rescale (*59*) for temperature coupling and Parrinello-Rahman barostat for pressure coupling. Semi-isotropic pressure coupling was used during simulation. All bounds involving hydrogen atoms were constrained using LINCS algorithm. Short-range nonbonded interactions were cut at 12 Å. Long-range electrostatic interactions were computed using particle mesh Ewald summation with a Fourier grid spacing of 1.6 Å. The production run was performed with the same parameters as described above but with the thermostat switched to Nose-Hoover (*60*).

The resulting production trajectories were analyzed using VMD (*61*), and PyMOL was also used to generate the images. RMSDs of the protein Cα atoms and cis-22a heavy atoms were calculated following superposition of residues of each tetramer subunit onto the coordinates of the energy-minimized structure.

Cadmium influx assay (FLIPR)

Molecular biology

The hTRPV6 mutants were constructed by site-directed mutagenesis (SDM) of hTRPV6 pIRES2 DsRed-Express2 or TagRFP-hTRPV6 pTagRFP-C1 construct using Pfu Turbo DNA polymerase (Agilent Technologies). The forward mutagenesis primers used for SDM were synthesized by Microsynth AG (Balgach, Switzerland). The reverse complementary of the primers was used as the reverse mutagenesis primers. The correct clones were verified by Sanger sequencing (Microsynth AG).

hTRPV6 functional assay on FLIPR

HEK 293 cells (ATCC CRL-3216) were seeded at a density of 30,000 cells per well on poly-D-lysine (P6407, Sigma-Aldrich)–coated Corning 96-well black polystyrene clear bottom microplates (CLS3603, Sigma-Aldrich) in 100 μl of phenol red–free Dulbecco's modified Eagle's medium (DMEM) supplemented with 10% FBS without antibiotics. The cells were cultured at 37°C and 5% CO_2 until 80 to 90% confluent (16 to 20 hours), after which they were transfected with 200 ng of plasmid DNA (wild-type or mutant hTRPV6) per well using Lipofectamine 2000 (11668019, Thermo Fisher Scientific).

One vial of calcium indicator, calcium-5 (R8186, Molecular Devices LLC), was reconstituted with 10 ml of nominally calcium-free (NCF) modified Krebs buffer containing 117 mM NaCl, 4.8 mM KCl, 1 mM $MgCl_2$, 10 mM D-glucose, and 10 mM Hepes (pH 7.5). Sixteen to 18 hours after transfections, cells were washed with NCF Krebs buffer (250 μl per well) and loaded (90 μl per well) with NCF Krebs buffer containing 50 μl of reconstituted calcium-5 indicator per milliliter of buffer. Following 1-hour incubation at 37°C in the dark, fluorescence measurements were carried out using a fluorometric imaging plate reader, FLIPR Tetra (Molecular Devices, LLC), to assess the effect of different mutations or inhibitors on TRPV6 channel function. During the FLIPR assay, the cells were illuminated using a 470- to 495-nm light-emitting diode module, and the emitted fluorescence signal was filtered with a 515- to 575-nm emission filter. After recording a 50-s baseline, 10 μl of 10X (X, final concentration) TRPV6 inhibitor dissolved in NCF Krebs buffer was robotically administered to the cells. Cells were incubated, and fluorescence was monitored in the presence of the inhibitor for a total of 10 min before the administration of 100 μM (2X) $CdCl_2$ dissolved in NCF Krebs buffer. The fluorescence was monitored for another 5 min after administration of $CdCl_2$. The fluorescence signals were analyzed using the ScreenWorks 3.1.1.8 software (Molecular Devices LLC). The TRPV6-mediated Cd^{2+} influx was quantified by calculating the area under the curve (AUC) of the fluorescence intensity traces, following administration of the final 50 μM $CdCl_2$. The AUC of the empty vector–transfected cells was used for background subtraction. Data from at least two independent experiments are presented. The Br-cis-22a dose-response curves were generated (nine-point curve, six repeats per concentration, twofold serial dilution starting at 10 μM), and the IC_{50} values were extrapolated from these plots for each compound (GraphPad Prism, version 5.0). Inhibition curves were obtained by nonlinear regression using the built-in log[inhibitor] versus response variable-slope function (four parameters).

Electrophysiology

Cell culture, construct, and molecular biology

HEK 293 cells were cultured in DMEM supplemented with 10% fetal calf serum, penicillin (100 U/ml), and streptomycin (100 μg/ml) at 37°C under humidified atmosphere containing 5% CO_2, as previously described. The cells were transiently transfected 24 hours before the experiments with human or rat TRPV6 N-terminally tagged with eYFP (enhanced yellow fluorescent protein) (peYFP vector) using TransFectin Lipid reagent (Bio-Rad). The endogenous TRPV6 protein in human comprises an extended N terminus (765 amino acids); however, for all experiments in this publication, the truncated version (725 amino acids) of the TRPV6 channel was used. Mutations in hTRPV6 (N464L, R470A, Q483A, F504Y, W583F, R470A, and W583F) were generated using the QuikChange XL SDM kit (Stratagene) and were confirmed by sequencing.

Electrophysiological recordings

Patch-clamp experiments were conducted in the whole-cell configuration at r.t. (20° to 24°C) with an Ag/AgCl reference electrode. Voltage ramps ranging from −90 to +90 mV over a time period of 200 ms were applied every 5 s from the holding potential of 50 mV. For the time courses, the inward current density was recorded at −74 mV. The internal pipette solution contained the following: 145 mM Cs-methanesulfonate, 8 mM NaCl, 5 mM $MgCl_2$, 10 mM Hepes, and 20 mM EGTA (pH 7.2). The extracellular solution (10 mM Ca^{2+}) consisted of 145 mM NaCl, 5 mM CsCl,1 mM $MgCl_2$, 10 mM Hepes, 10 mM glucose, and 10 mM $CaCl_2$ (pH 7.4). The DVF solution comprised 150 mM NaCl, 10 mM Hepes, 10 mM glucose, and 10 mM EDTA (pH 7.4). The currents were leak-corrected by subtraction of the remaining leak currents after 100 μM or 1 mM $LaCl_3$ block. The liquid junction potential was determined as 12 mV; the voltages were not adjusted. All experiments were conducted for a minimum of two different experimental days. Application of the same amount of DMSO in 10 mM Ca^{2+} solution as in the inhibitor-containing solution was used as a control. Statistical analyses and

graphs (means ± SEM) were done using the OriginPro software (version 9.1, for Windows, OriginLab). The results were assumed to follow the normal distribution, and the hypothesis testing was performed using either two-sided Student's paired or unpaired *t* tests, Wilcoxon signed-rank tests (two-sided), or Mann-Whitney *U* tests. * indicates significance (P value < 0.05); ns stands for "not significant." Dose-response curves were fitted with the Hill equation, and the extent of calcium-dependent inactivation was measured as the current amplitude reduction after 180 s since the beginning of calcium application relative to the maximum current amplitude.

SUPPLEMENTARY MATERIALS

Supplementary material for this article is available at http://advances.sciencemag.org/cgi/content/full/6/48/eabe1508/DC1

REFERENCES AND NOTES

1. D. E. Clapham, TRP channels as cellular sensors. *Nature* **426**, 517–524 (2003).
2. B. Nilius, A. Szallasi, Transient receptor potential channels as drug targets: From the science of basic research to the art of medicine. *Pharmacol. Rev.* **66**, 676–814 (2014).
3. M. V. Yelshanskaya, K. D. Nadezhdin, M. G. Kurnikova, A. I. Sobolevsky, Structure and function of the calcium-selective TRP channel TRPV6. *J. Physiol.*, https://doi.org/10.1113/JP279024 (2020).
4. S. D. Bianco, J. B. Peng, H. Takanaga, Y. Suzuki, A. Crescenzi, C. H. Kos, L. Zhuang, M. R. Freeman, C. H. Gouveia, J. Wu, H. Luo, T. Mauro, E. M. Brown, M. A. Hediger, Marked disturbance of calcium homeostasis in mice with targeted disruption of the Trpv6 calcium channel gene. *J. Bone Miner. Res.* **22**, 274–285 (2007).
5. Y. Suzuki, C. S. Kovacs, H. Takanaga, J. B. Peng, C. P. Landowski, M. A. Hediger, Calcium channel TRPV6 is involved in murine maternal-fetal calcium transport. *J. Bone Miner. Res.* **23**, 1249–1256 (2008).
6. L. Lieben, B. S. Benn, D. Ajibade, I. Stockmans, K. Moermans, M. A. Hediger, J. B. Peng, S. Christakos, R. Bouillon, G. Carmeliet, Trpv6 mediates intestinal calcium absorption during calcium restriction and contributes to bone homeostasis. *Bone* **47**, 301–308 (2010).
7. Y. Suzuki, D. Chitayat, H. Sawada, M. A. Deardorff, H. M. McLaughlin, A. Begtrup, K. Millar, J. Harrington, K. Chong, M. Roifman, K. Grand, M. Tominaga, F. Takada, S. Shuster, M. Obara, H. Mutoh, R. Kushima, G. Nishimura, TRPV6 variants interfere with maternal-fetal calcium transport through the placenta and cause transient neonatal hyperparathyroidism. *Am. J. Hum. Genet.* **102**, 1104–1114 (2018).
8. C. P. Burren, R. Caswell, B. Castle, C. R. Welch, T. N. Hilliard, S. F. Smithson, S. Ellard, TRPV6 compound heterozygous variants result in impaired placental calcium transport and severe undermineralization and dysplasia of the fetal skeleton. *Am. J. Med. Genet. A* **176**, 1950–1955 (2018).
9. J. M. Stewart, TRPV6 as A Target for Cancer Therapy. *J. Cancer* **11**, 374–387 (2020).
10. S. M. Huber, Oncochannels. *Cell Calcium* **53**, 241–255 (2013).
11. J. B. Peng, Y. Suzuki, G. Gyimesi, M. A. Hediger, TRPV5 and TRPV6 calcium-selective channels, in *Calcium Entry Channels in Non-Excitable Cells,* J. A. Kozak, J. W. Putney Jr., Eds. (CRC Press/Taylor & Francis, 2018), pp. 241–274.
12. I. Dhennin-Duthille, M. Gautier, M. Faouzi, A. Guilbert, M. Brevet, D. Vaudry, A. Ahidouch, H. Sevestre, H. Ouadid-Ahidouch, High expression of transient receptor potential channels in human breast cancer epithelial cells and tissues: Correlation with pathological parameters. *Cell. Physiol. Biochem.* **28**, 813–822 (2011).
13. E. C. Schwarz, U. Wissenbach, B. A. Niemeyer, B. Strauss, S. E. Philipp, V. Flockerzi, M. Hoth, TRPV6 potentiates calcium-dependent cell proliferation. *Cell Calcium* **39**, 163–173 (2006).
14. V. Lehen'kyi, M. Flourakis, R. Skryma, N. Prevarskaya, TRPV6 channel controls prostate cancer cell proliferation via Ca^{2+}/NFAT-dependent pathways. *Oncogene* **26**, 7380–7385 (2007).
15. K. A. Bolanz, M. A. Hediger, C. P. Landowski, The role of TRPV6 in breast carcinogenesis. *Mol. Cancer Ther.* **7**, 271–279 (2008).
16. C. V. Bowen, D. DeBay, H. S. Ewart, P. Gallant, S. Gormley, T. T. Ilenchuk, U. Iqbal, T. Lutes, M. Martina, G. Mealing, N. Merkley, S. Sperker, M. J. Moreno, C. Rice, R. T. Syvitski, J. M. Stewart, In vivo detection of human TRPV6-rich tumors with anti-cancer peptides derived from soricidin. *PLOS ONE* **8**, e58866 (2013).
17. D. M. Haverstick, T. N. Heady, T. L. Macdonald, L. S. Gray, Inhibition of human prostate cancer proliferation in vitro and in a mouse model by a compound synthesized to block Ca^{2+} entry. *Cancer Res.* **60**, 1002–1008 (2000).
18. C. P. Landowski, K. A. Bolanz, Y. Suzuki, M. A. Hediger, Chemical inhibitors of the calcium entry channel TRPV6. *Pharm. Res.* **28**, 322–330 (2011).
19. G. Kovacs, N. Montalbetti, A. Simonin, T. Danko, B. Balazs, A. Zsembery, M. A. Hediger, Inhibition of the human epithelial calcium channel TRPV6 by 2-aminoethoxydiphenyl borate (2-APB). *Cell Calcium* **52**, 468–480 (2012).
20. A. Hofer, G. Kovacs, A. Zappatini, M. Leuenberger, M. A. Hediger, M. Lochner, Design, synthesis and pharmacological characterization of analogs of 2-aminoethyl diphenylborinate (2-APB), a known store-operated calcium channel blocker, for inhibition of TRPV6-mediated calcium transport. *Bioorg. Med. Chem.* **21**, 3202–3213 (2013).
21. C. Simonin, M. Awale, M. Brand, R. van Deursen, J. Schwartz, M. Fine, G. Kovacs, P. Hafliger, G. Gyimesi, A. Sithampari, R.-P. Charles, M. A. Hediger, J.-L. Reymond, Optimization of TRPV6 calcium channel inhibitors using a 3D ligand-based virtual screening method. *Angew. Chem. Int. Ed. Engl.* **54**, 14748–14752 (2015).
22. M. R. Cunha, R. Bhardwaj, S. Lindinger, C. Butorac, C. Romanin, M. A. Hediger, J.-L. Reymond, Photoswitchable inhibitor of the calcium channel TRPV6. *ACS Med. Chem. Lett.* **10**, 1341–1345 (2019).
23. M. R. Cunha, R. Bhardwaj, A. L. Carrel, S. Lindinger, C. Romanin, R. Parise-Filho, M. A. Hediger, J.-L. Reymond, Natural product inspired optimization of a selective TRPV6 calcium channel inhibitor. *RSC Med. Chem.* **11**, 1032–1040 (2020).
24. C. Cao, E. Zakharian, I. Borbiro, T. Rohacs, Interplay between calmodulin and phosphatidylinositol 4,5-bisphosphate in Ca^{2+}-induced inactivation of transient receptor potential vanilloid 6 channels. *J. Biol. Chem.* **288**, 5278–5290 (2013).
25. I. Derler, M. Hofbauer, H. Kahr, R. Fritsch, M. Muik, K. Kepplinger, M. E. Hack, S. Moritz, R. Schindl, K. Groschner, C. Romanin, Dynamic but not constitutive association of calmodulin with rat TRPV6 channels enables fine tuning of Ca2+–dependent inactivation. *J. Physiol.* **577**, 31–44 (2006).
26. K. Saotome, A. K. Singh, M. V. Yelshanskaya, A. I. Sobolevsky, Crystal structure of the epithelial calcium channel TRPV6. *Nature* **534**, 506–511 (2016).
27. A. K. Singh, K. Saotome, A. I. Sobolevsky, Swapping of transmembrane domains in the epithelial calcium channel TRPV6. *Sci. Rep.* **7**, 10669 (2017).
28. K. Saotome, A. K. Singh, A. I. Sobolevsky, Determining the crystal structure of TRPV6, in *Calcium Entry Channels in Non-Excitable Cells,* J. A. Kozak, J. W. Putney Jr., Eds. (CRC Press/Taylor & Francis, 2018), pp. 275–292.
29. A. K. Singh, K. Saotome, L. L. McGoldrick, A. I. Sobolevsky, Structural bases of TRP channel TRPV6 allosteric modulation by 2-APB. *Nat. Commun.* **9**, 2465 (2018).
30. A. K. Singh, L. L. McGoldrick, E. C. Twomey, A. I. Sobolevsky, Mechanism of calmodulin inactivation of the calcium-selective TRP channel TRPV6. *Sci. Adv.* **4**, eaau6088 (2018).
31. L. L. McGoldrick, A. K. Singh, K. Saotome, M. V. Yelshanskaya, E. C. Twomey, R. A. Grassucci, A. I. Sobolevsky, Opening of the human epithelial calcium channel TRPV6. *Nature* **553**, 233–237 (2018).
32. Y. Gao, E. Cao, D. Julius, Y. Cheng, TRPV1 structures in nanodiscs reveal mechanisms of ligand and lipid action. *Nature* **534**, 347–351 (2016).
33. E. Cao, M. Liao, Y. Cheng, D. Julius, TRPV1 structures in distinct conformations reveal activation mechanisms. *Nature* **504**, 113–118 (2013).
34. A. K. Singh, L. L. McGoldrick, L. Demirkhanyan, M. Leslie, E. Zakharian, A. I. Sobolevsky, Structural basis of temperature sensation by the TRP channel TRPV3. *Nat. Struct. Mol. Biol.* **26**, 994–998 (2019).
35. A. K. Singh, L. L. McGoldrick, A. I. Sobolevsky, Structure and gating mechanism of the transient receptor potential channel TRPV3. *Nat. Struct. Mol. Biol.* **25**, 805–813 (2018).
36. J. van der Wijst, E. H. Leunissen, M. G. Blanchard, H. Venselaar, S. Verkaart, C. E. Paulsen, R. J. Bindels, J. G. Hoenderop, A gate hinge controls the epithelial calcium channel TRPV5. *Sci. Rep.* **7**, 45489 (2017).
37. T. E. T. Hughes, R. A. Pumroy, A. T. Yazici, M. A. Kasimova, E. C. Fluck, K. W. Huynh, A. Samanta, S. K. Molugu, Z. H. Zhou, V. Carnevale, T. Rohacs, V. Y. Moiseenkova-Bell, Structural insights on TRPV5 gating by endogenous modulators. *Nat. Commun.* **9**, 4198 (2018).
38. S. Dang, M. K. van Goor, D. Asarnow, Y. Wang, D. Julius, Y. Cheng, J. van der Wijst, Structural insight into TRPV5 channel function and modulation. *Proc. Natl. Acad. Sci. U.S.A.* **116**, 8869–8878 (2019).
39. K. E. Huffer, A. A. Aleksandrova, A. Jara-Oseguera, L. R. Forrest, K. J. Swartz, Global alignment and assessment of TRP channel transmembrane domain structures to explore functional mechanisms. *eLife* **9**, e58660 (2020).
40. M. M. Diver, Y. Cheng, D. Julius, Structural insights into TRPM8 inhibition and desensitization. *Science* **365**, 1434–1440 (2019).
41. R. A. Pumroy, A. Samanta, Y. Liu, T. E. Hughes, S. Zhao, Y. Yudin, T. Rohacs, S. Han, V. Y. Moiseenkova-Bell, Molecular mechanism of TRPV2 channel modulation by cannabidiol. *eLife* **8**, e48792 (2019).
42. T. E. T. Hughes, D. T. Lodowski, K. W. Huynh, A. Yazici, J. Del Rosario, A. Kapoor, S. Basak, A. Samanta, X. Han, S. Chakrapani, Z. H. Zhou, M. Filizola, T. Rohacs, S. Han, V. Y. Moiseenkova-Bell, Structural basis of TRPV5 channel inhibition by econazole revealed by cryo-EM. *Nat. Struct. Mol. Biol.* **25**, 53–60 (2018).
43. A. Goehring, C. H. Lee, K. H. Wang, J. C. Michel, D. P. Claxton, I. Baconguis, T. Althoff, S. Fischer, K. C. Garcia, E. Gouaux, Screening and large-scale expression of membrane proteins in mammalian cells for structural studies. *Nat. Protoc.* **9**, 2574–2585 (2014).

44. W. Kabsch, Xds. *Acta Crystallogr. D Biol. Crystallogr.* **66**, 125–132 (2010).
45. A. J. McCoy, R. W. Grosse-Kunstleve, P. D. Adams, M. D. Winn, L. C. Storoni, R. J. Read, Phaser crystallographic software. *J. Appl. Cryst.* **40**, 658–674 (2007).
46. P. V. Afonine, R. W. Grosse-Kunstleve, N. Echols, J. J. Headd, N. W. Moriarty, M. Mustyakimov, T. C. Terwilliger, A. Urzhumtsev, P. H. Zwart, P. D. Adams, Towards automated crystallographic structure refinement with phenix.refine. *Acta Crystallogr. D* **68**, 352–367 (2012).
47. P. Emsley, B. Lohkamp, W. G. Scott, K. Cowtan, Features and development of Coot. *Acta Crystallogr. D Biol. Crystallogr.* **66**, 486–501 (2010).
48. C. J. Russo, L. A. Passmore, Ultrastable gold substrates for electron cryomicroscopy. *Science* **346**, 1377–1380 (2014).
49. C. Suloway, J. Pulokas, D. Fellmann, A. Cheng, F. Guerra, J. Quispe, S. Stagg, C. S. Potter, B. Carragher, Automated molecular microscopy: The new Leginon system. *J. Struct. Biol.* **151**, 41–60 (2005).
50. S. H. Scheres, RELION: Implementation of a Bayesian approach to cryo-EM structure determination. *J. Struct. Biol.* **180**, 519–530 (2012).
51. A. Punjani, J. L. Rubinstein, D. J. Fleet, M. A. Brubaker, cryoSPARC: Algorithms for rapid unsupervised cryo-EM structure determination. *Nat. Methods* **14**, 290–296 (2017).
52. S. Q. Zheng, E. Palovcak, J.-P. Armache, K. A. Verba, Y. Cheng, D. A. Agard, MotionCor2: Anisotropic correction of beam-induced motion for improved cryo-electron microscopy. *Nat. Methods* **14**, 331–332 (2017).
53. K. Zhang, Gctf: Real-time CTF determination and correction. *J. Struct. Biol.* **193**, 1–12 (2016).
54. E. F. Pettersen, T. D. Goddard, C. C. Huang, G. S. Couch, D. M. Greenblatt, E. C. Meng, T. E. Ferrin, UCSF Chimera—A visualization system for exploratory research and analysis. *J. Comput. Chem.* **25**, 1605–1612 (2004).
55. K. Goossens, H. De Winter, Molecular dynamics simulations of membrane proteins: An overview. *J. Chem. Inf. Model.* **58**, 2193–2202 (2018).
56. D. Van Der Spoel, E. Lindahl, B. Hess, G. Groenhof, A. E. Mark, H. J. Berendsen, GROMACS: Fast, flexible, and free. *J. Comput. Chem.* **26**, 1701–1718 (2005).
57. C. Kandt, W. L. Ash, D. P. Tieleman, Setting up and running molecular dynamics simulations of membrane proteins. *Methods* **41**, 475–488 (2007).
58. O. Berger, O. Edholm, F. Jahnig, Molecular dynamics simulations of a fluid bilayer of dipalmitoylphosphatidylcholine at full hydration, constant pressure, and constant temperature. *Biophys. J.* **72**, 2002–2013 (1997).
59. G. Bussi, D. Donadio, M. Parrinello, Canonical sampling through velocity rescaling. *J. Chem. Phys.* **126**, 014101 (2007).
60. W. G. Hoover, Canonical dynamics: Equilibrium phase-space distributions. *Phys. Rev. A* **31**, 1695–1697 (1985).
61. W. Humphrey, A. Dalke, K. Schulten, VMD: Visual molecular dynamics. *J. Mol. Graph.* **14**, 33–38 (1996).
62. O. S. Smart, J. G. Neduvelil, X. Wang, B. A. Wallace, M. S. Samsom, HOLE: A program for the analysis of the pore dimensions of ion channel structural models. *J. Mol. Graph.* **14**, 354–360 (1996).

Acknowledgments: We thank R. Grassucci, Z. Zhang, Y.-C. Chi, and L. Zheng for help with microscope operation and data collection; H. Kao for computational support; and S. Buchegger for excellent technical assistance. **Funding:** A.I.S. was supported by the NIH (R01 CA206573, R01 NS083660, and R01 NS107253), NSF (1818086), and the Irma T. Hirschl Career Scientist Award. Data were collected at the Columbia University Cryo-EM Facility and at the Simons Electron Microscopy Center and National Resource for Automated Molecular Microscopy (New York Structural Biology Center) supported by grants from the Simons Foundation (349247), NYSTAR, and the NIH (GM103310). X-ray diffraction data collection was conducted at the Northeastern Collaborative Access Team beamlines, which are funded by the National Institute of General Medical Sciences from the National Institutes of Health (P30 GM124165). The Pilatus 6M detector on the 24-ID-C beam line is funded by a NIH-ORIP HEI grant (S10 RR029205). This research used resources of the Advanced Photon Source, a U.S. Department of Energy (DOE) Office of Science User Facility operated for the DOE Office of Science by Argonne National Laboratory under contract no. DE-AC02-06CH11357. This work was also supported, in part, by the Linz Institute of Technology project LIT-2018-05-SEE-111 (to I.D.) and Austrian Science Funds FWF P33283 (to C.R.). R.B. and M.A.H. were supported by the SNF Sinergia grants CRSII5_180326 and CRSII3_160782. M.R.C. was supported by the Swiss Excellence Scholarship for Foreign Students and Scholars (ESKAS, 2017.0670).

Author contributions: A.N., K.D.N., and A.K.S. made constructs, prepared protein samples, and carried out crystallographic and cryo-EM data collection and processing. A.N., K.D.N., A.K.S., and A.I.S. analyzed structural data. S.L. prepared constructs and performed and analyzed electrophysiological experiments. I.D. and C.R. designed the electrophysiology experiments. R.B. and G.G. constructed TRPV6 mutants and performed and analyzed the FLIPR experiments. M.R.C. synthesized cis-22a and its derivatives and performed FLIPR testing of Br-cis-22a and molecular dynamics simulations. R.B., S.L., A.N., K.D.N., A.K.S., M.R.C., I.D., J.-L.R., M.A.H., C.R., and A.I.S. wrote the manuscript. **Competing interests:** The authors declare that they have no competing interests. **Data and materials availability:** All data needed to evaluate the conclusions of the paper are present in the paper and/or the Supplementary Materials. Additional data related to this paper may be requested from the authors. The atomic coordinates and structure factors for the TRPV6*–Br-cis-22a crystal structure have been deposited to the Protein Data Bank (PDB) under the accession code 7D2K (see table S1 for details). Cryo-EM density maps have been deposited to the Electron Microscopy Data Bank (EMDB) under the accession codes EMDB-22662 (hTRPV6-CtD-apo), EMDB-22663 (hTRPV6-CtD-cis-22a), EMDB-22664 (hTRPV6-CtD-Br-cis-22a), EMDB-22665 (hTRPV6-CtD-3OG), EMDB-22666 (hTRPV6-CtD-30), and EMDB-22667 (hTRPV6-CtD-31) (see table S2 for details). The corresponding model coordinates have been deposited to the PDB under accession numbers 7K4A (hTRPV6-CtD-apo), 7K4B (hTRPV6-CtD-cis-22a), 7K4C (hTRPV6-CtD-Br-cis-22a), 7K4D (hTRPV6-CtD-3OG), 7K4E (hTRPV6-CtD-30), and 7K4F (hTRPV6-CtD-31) (see table S2 for details).

Submitted 3 August 2020
Accepted 14 October 2020
Published 27 November 2020
10.1126/sciadv.abe1508

Citation: R. Bhardwaj, S. Lindinger, A. Neuberger, K. D. Nadezhdin, A. K. Singh, M. R. Cunha, I. Derler, G. Gyimesi, J.-L. Reymond, M. A. Hediger, C. Romanin, A. I. Sobolevsky, Inactivation-mimicking block of the epithelial calcium channel TRPV6. *Sci. Adv.* **6**, eabe1508 (2020).

Science Advances

Inactivation-mimicking block of the epithelial calcium channel TRPV6

Rajesh Bhardwaj, Sonja Lindinger, Arthur Neuberger, Kirill D. Nadezhdin, Appu K. Singh, Micael R. Cunha, Isabella Derler, Gergely Gyimesi, Jean-Louis Reymond, Matthias A. Hediger, Christoph Romanin and Alexander I. Sobolevsky

Sci Adv **6** (48), eabe1508.
DOI: 10.1126/sciadv.abe1508